A&A, 709, A82 (2026)
https://doi.org/10.1051/0004-6361/202558581

Astronomy & Astrophysics

KiDS-Legacy: Constraining dark energy, neutrino mass, and curvature

Robert Reischke[1,2,⋆], Benjamin Stölzner[2], Benjamin Joachimi[3], Angus H. Wright[2], Marika Asgari[4], Maciej Bilicki[5], Nora Elisa Chisari[6,7], Andrej Dvornik[2], Christos Georgiou[8], Benjamin Giblin[9], Joachim Harnois-Déraps[4], Catherine Heymans[2,9], Hendrik Hildebrandt[2], Henk Hoekstra[7], Shahab Joudaki[10], Konrad Kuijken[7], Shun-Sheng Li[11,12], Laila Linke[13], Arthur Loureiro[14,15], Constance Mahony[16,17,2], Lauro Moscardini[18,19,20], Nicola R. Napolitano[21], Lucas Porth[1], Mario Radovich[22], Tilman Tröster[23], Maximilian von Wietersheim-Kramsta[24,25], Ziang Yan[2,26], Mijin Yoon[7], and Yun-Hao Zhang[7,9]

(Affiliations can be found after the references)

Received 15 December 2025 / Accepted 17 March 2026

ABSTRACT

We constrained minimally extended cosmological models with the cosmic shear analysis of the final data release from the Kilo-Degree Survey (KiDS-Legacy) in combination with external probes. Due to the consistency of the KiDS-Legacy analysis with the cosmic microwave background (CMB), we could combine these datasets reliably for the first time. Additionally, we used CMB lensing, galaxy redshift-space distortions, and baryon acoustic oscillations. We assessed, in turn, the effects of spatial curvature, varying neutrino masses, and an evolving dark energy component on cosmological constraints from KiDS-Legacy alone and from KiDS-Legacy combined with external probes. We find KiDS-Legacy to be consistent with the fiducial flat Λ-cold dark matter (ΛCDM) analysis with $c^2 \sum m_\nu \leq 1.5\,\mathrm{eV}$, $w_0 = -1.0 \pm 0.7$, and $w_a = -1.3^{+1.9}_{-2.0}$ while $\Omega_K = 0.08^{+0.16}_{-0.17}$ (1σ bounds) with an almost equal goodness of fit. The $w_0 w_a$CDM model is not a significant improvement over ΛCDM when cosmic shear and CMB lensing are combined, yielding a Bayes factor $B = 0.07$. If all probes are combined, however, B increases to 2.73, corresponding to a 2.6σ suspiciousness tension. The constraint on $S_8 = \sigma_8 \sqrt{\Omega_\mathrm{m}/0.3}$ is robust to opening up the parameter space for cosmic shear. Adding all external datasets to KiDS-Legacy, we find $S_8 = 0.816 \pm 0.006$ in ΛCDM and $S_8 = 0.837 \pm 0.008$ in $w_0 w_a$CDM for all probes combined.

Key words. cosmological parameters – cosmology: observations – cosmology: theory – dark energy – large-scale structure of Universe

1. Introduction

The model currently best capturing the dynamics of the Universe on large scales is the Λ-cold dark matter model with vanishing spatial curvature (flat ΛCDM). Despite some discrepancies, this simple model with only a few parameters successfully explains a wide range of observations.

The weak gravitational lensing effect of the large-scale structure (LSS), also known as cosmic shear, has become a staple cosmological observable since its first detection over two decades ago (Kaiser et al. 2000; Wittman et al. 2000; Van Waerbeke et al. 2000; Bacon et al. 2000). Due to its sensitivity to the growth of structure as well as the background cosmology, it has the potential to probe the ΛCDM model and its extensions. The most recent analysis comes from the so-called Stage-III weak lensing surveys, the Kilo-Degree Survey (KiDS, see Wright et al. 2025b; Stölzner et al. 2025, for the most recent analysis)[1], the Dark Energy Survey (DES, see e.g. Amon et al. 2022; Secco et al. 2022; Samuroff et al. 2023)[2], and the Subaru Hyper Suprime-Cam Subaru Strategic Project (HSC, see e.g. Li et al. 2023c; Dalal et al. 2023[3]). Cosmic shear is joined by other probes such as the cosmic microwave background (CMB; Planck Collaboration VI 2020; Camphuis et al. 2025; Louis et al. 2025), baryon acoustic oscillations (BAOs; Adame et al. 2025; Desi & Abdul-Karim 2025; Alam et al. 2021), redshift space distortion (RSD; Hou et al. 2021), expansion history measurements via Type Ia supernovae (SNeIa; Scolnic et al. 2022; Brout et al. 2022), as well as the present-day expansion rate, that is the Hubble constant, through Cepheids (Riess et al. 2019), strongly lensed quasars (Wong et al. 2020), or the tip of the red giant branch and J-region asymptotic giant branch stars (see Freedman et al. 2025, for an overview). These last measurements technically do not depend on cosmology, as they are local and thus cannot distinguish between different cosmological models beyond the overall normalisation of the expansion rate.

The first direct evidence of the accelerated expansion of the Universe (Riess et al. 1998; Schmidt et al. 1998; Perlmutter et al. 1999) established cosmological probes across cosmic time as a test bed for physics beyond the standard model. These measurements implied, in hindsight, an unsurprisingly non-vanishing second coupling constant, Λ, in the gravity sector. One can express Λ itself as an ideal fluid with constant energy density and with negative pressure. More generally, one can relate the energy density to the pressure via an equation of state, $w\,[a(z)]$, which can depend on redshift z. This dynamic scenario can itself originate from an additional field that acts solely on the background cosmology and does not form perturbations. A key target of cosmology is therefore to use cosmological observables to infer $w(a)$ and test whether it assumes its ΛCDM value of $w = -1$. Many constraints on w use an expansion up to linear order, which effectively approximates many different dark energy models (Chevallier & Polarski 2001; Linder

⋆ Corresponding author: rreischk@uni-bonn.de, reischke@posteo.net

[1] https://kids.strw.leidenuniv.nl/
[2] https://www.darkenergysurvey.org
[3] https://hsc.mtk.nao.ac.jp/ssp/

Table 1. Data combinations used in this analysis. The details are described in Sect. 2.

Name	Dataset
KiDS	KiDS DR5 cosmic shear catalogue
CMB	SPT-3G D1 + ACT DR6 + Planck 2018 Lensing and primary (also known as SPA)
Lensing	KiDS + DES Y3 + CMBlensing
Low-z	KiDS + DES Y3 + DESI DR2 BAO + eBOSS DR16 RSD

Notes. With low-z we refer to all probes which are entirely based on observations at low redshift. Therefore, the lensing signal of the CMB is not included in the low-z set.

2003). Recently, the Dark Energy Spectroscopic Instrument (DESI Adame et al. 2025; Desi & Abdul-Karim 2025) found tentative evidence that $w \neq -1$ in this parametrisation using BAO measurements and external probes including the CMB. This modification of the expansion history becomes particularly interesting in light of the Hubble tension, the discrepancy between local and early time measurements of the expansion rate (see e.g. Schöneberg et al. 2022; Kamionkowski & Riess 2023; Di Valentino et al. 2025, for reviews and summaries).

While Wright et al. (2025b) and Stölzner et al. (2025) recently put forward constraints on flat ΛCDM using the final data release of KiDS (DR5; Wright et al. 2024), the goal of this paper is to expand this analysis to minimal extensions to the baseline cosmological model and include external datasets. Unlike in the previous KiDS analyses (KiDS-1000 and its reanalyses; Asgari et al. 2021; Tröster et al. 2021; van den Busch et al. 2022; Li et al. 2023a; Yoon et al. 2025), which found a tension in the amount of matter clustering in the Universe compared to the CMB (the S_8 tension), KiDS-Legacy is consistent with the other cosmological observables. The driving contributing factors are updated redshift calibration and scale cuts (see Appendix I in Wright et al. 2025b). This consistency allows the combination of different probes and opens the possibility of constraining extended parameter spaces.

On the data side, we used CMB primary anisotropies from Planck (Planck Collaboration V 2020), the Atacama Cosmology Telescope (ACT; Louis et al. 2025), and the South Pole Telescope (SPT; Camphuis et al. 2025), the signal from gravitational lensing of the CMB (Planck Collaboration V 2020; Madhavacheril et al. 2024; Ge et al. 2025), BAO data from DESI (Desi & Abdul-Karim 2025), RSD from the Extended Baryon Oscillation Spectroscopic Survey (eBOSS, e.g. Hou et al. 2021), SNeIa from the Pantheon+ sample (Scolnic et al. 2022), and combined cosmic shear measurements from KiDS-Legacy and DES Y3 based on Dark Energy Survey and Kilo-Degree Survey Collaboration (2023) with the updated data from Wright et al. (2024). For the modelling, we focused on three main extensions to the fiducial analysis: (i) varying neutrino mass ($\nu\Lambda$CDM), (ii) dynamic dark energy (w_0w_aCDM), and (iii) a spatially non-flat Universe (Ω_KCDM). Although the linear growth factor is modified in dynamic dark energy scenarios, the extensions studied here do not explicitly alter the gravity sector; that is, we assume general relativity throughout this paper and introduce no new gravitational fields. In a companion paper (Stölzner et al. 2026), we investigate, in more detail, extensions that alter the growth of structures by modifying the gravitational law in the context of Horndeski theory.

We structure this paper as follows: Sect. 2 briefly summarises the methodology, the inference pipeline, data, and likelihood used in this analysis. In Sect. 3, we present the results of the three types of extended models for different probe combinations. Lastly, we summarise our findings and conclude in Sect. 4.

2. Methodology and datasets

In this section, we first briefly summarise the methodology used for the cosmic shear analysis, which follows the one used in Wright et al. (2025b), Stölzner et al. (2025), Reischke et al. (2025).

2.1. Cosmic shear and KiDS-Legacy

The KiDS-Legacy dataset combines two European Southern Observatory Public Surveys: KiDS (de Jong et al. 2013) on the VLT Survey Telescope (VST) and on the VISTA telescope, the VISTA Kilo-Degree Infrared Galaxy Survey (VIKING; Edge et al. 2013). The KiDS data span $1,347\,\mathrm{deg}^2$ in two stripes on and south of the celestial equator, with optical bands u, g, r, i from VST and Z, Y, J, H, K_s from VIKING. Compared with the previous release, DR5 adds a second i-band pass and increases the area by 34 per cent. The KiDS-Legacy lensing catalogue contains 41 million source galaxies over $967\,\mathrm{deg}^2$, with an effective number density of $8.79\,\mathrm{arcmin}^{-2}$. Deeper i-band imaging and expanded spectroscopic calibration allow a higher photometric redshift limit of $z_B \leq 2$ and an extra high redshift tomographic bin. Sources are split into six roughly equally-populated bins by photometric redshifts, and the corresponding redshift distributions are calibrated against deep spectroscopy using self-organising maps and the multicolour SKiLLS simulations (see Li et al. 2023b; Wright et al. 2025a, for details). Galaxy shapes were measured with an updated version of the LENSFIT algorithm (Miller et al. 2013; Fenech Conti et al. 2017) and calibrated with SKiLLS.

We use CosmoPipe[4] for the cosmic shear measurement, calibration, and inference infrastructure. As the summary statistic, we use the first six modes of the complete orthogonal sets of E/B-integrals (COSEBIs; Schneider et al. 2010; Asgari et al. 2012), measured from 2 to 300 arcmin. The COSEBI E-modes are integrals over the angular power spectrum of the observed ellipticities, $C_{\epsilon\epsilon}^{(ij)}(\ell)$ in tomographic bins i and j, which in turn can be written as

$$C_{\epsilon\epsilon}^{(ij)}(\ell) = \int_0^{\chi_\mathrm{H}} \mathrm{d}\chi \, \frac{W_\epsilon^{(i)}(\chi) W_\epsilon^{(j)}(\chi)}{f_K^2(\chi)} P_\mathrm{m,nl}\left(\frac{\ell + 1/2}{f_K(\chi)}, z(\chi)\right). \quad (1)$$

Here, $P_\mathrm{m,nl}$ is the non-linear matter power spectrum, which we model using HMCODE2020 (Mead et al. 2021). This employs a single-parameter ($\log_{10} T_\mathrm{AGN}$) baryonic feedback model to include the uncertainty of the modelling of baryonic feedback on scales $k > 0.1h/\mathrm{Mpc}$. Furthermore, f_K, χ, and χ_H are the comoving angular diameter distance, the comoving radial distance, and the comoving horizon distance, respectively. Lastly, the lensing kernel $W_\epsilon^{(i)}$ contains the distribution of galaxies and the lensing geometry (see e.g. Wright et al. 2025b).

We adopt the fiducial mass-dependent intrinsic alignment (IA) model NLA-M (Wright et al. 2025b), an extension of the non-linear alignment (NLA) model that includes alignments for red, early-type galaxies and assumes zero alignment for

[4] https://github.com/AngusWright/CosmoPipe/tree/KiDSLegacy_CosmicShear

Table 2. Model parameters and their priors grouped by the concordance model, extensions, and nuisance.

Type	Parameter	Prior	Description
Flat ΛCDM	$\omega_{\rm cdm}$	$\mathcal{U}(0.051, 0.255)$	Cold dark matter density
	$\omega_{\rm b}$	$\mathcal{U}(0.019, 0.026)$	Baryon density
	h	$\mathcal{U}(0.64, 0.82)$	Reduced Hubble parameter
	$n_{\rm s}$	$\mathcal{U}(0.84, 1.1)$	Spectral index of the primordial power spectrum
	S_8	$\mathcal{U}(0.5, 1.0)$	Structure growth parameter
	$\ln 10^{10} A_{\rm s}$	$\mathcal{U}(2.9, 3.2)$	Matter power spectrum amplitude
Extended	$\sum m_\nu$[eV]	$\mathcal{U}(0, 3)$	Sum of the neutrino masses
	w_0	$\mathcal{U}(-3, 0)$	Dark energy equation of state today
	w_a	$\mathcal{U}(-5, 5)$	Linear slope of the dark energy equation of state
	Ω_K	$\mathcal{U}(-0.3, 0.3)$	Spatial curvature density parameter
Nuisance	$\log_{10} T_{\rm AGN}$	$\mathcal{U}(7.3, 8.3)$	Baryon feedback parameter
	$A_{\rm IA}$	$\mathcal{N}(5.74, \mathbf{C}_{A_{\rm IA},\beta})$	Amplitude of intrinsic galaxy alignments for red galaxies
	β	$\mathcal{N}(0.44, \mathbf{C}_{A_{\rm IA},\beta})$	Slope of the mass scaling of intrinsic galaxy alignments
	$\log_{10} M_{\rm i}$	$\mathcal{N}(\boldsymbol{\mu}, \mathbf{C}_M)$	Mean halo mass of early-type galaxies per tomographic bin i
	$\delta_{z,i}$	$\mathcal{N}(\boldsymbol{\mu}, \mathbf{C}_z)$	Shift of the mean of the redshift distribution per tomographic bin i

Notes. The first two columns specify the types of the sampling parameters and the parameter names, respectively. The third column gives the priors used, with uniform priors denoted by their interval $\mathcal{U}$, and Gaussian priors by $\mathcal{N}(\mu, \sigma)$. The fourth column offers a brief description of each parameter. For more details on the chosen priors, see Wright et al. (2025b), Stölzner et al. (2025), Wright et al. (2025a). For nuisance parameters of the external probes, we use the fiducial priors from the respective analyses. When including any CMB data, we sample over $\log A_{\rm s}$ instead of S_8 and derive S_8 instead. All constraints in Table 4 are, however, given in terms of S_8 only. We tested that this choice does not introduce any information and yields the same cosmological constraints.

blue, late-type galaxies. Wright et al. (2025b) investigated different alignment models and their impact on the inferred value for S_8, finding changes of not larger than 0.2σ. Our choice is further supported by a red-blue split analysis conducted by Stölzner et al. (2025), which found vanishing alignment for blue galaxies. Early types are identified by spectral type[5] $T_B < 1.9$, fitting six SED templates with interpolation; the cut selects galaxies with an elliptical spectral contribution. The IA alignment strength for red galaxies is modelled as a power law in the mean halo mass for each tomographic bin. We use two alignment parameters, $A_{\rm IA}$ and β, which represent the amplitude of IAs and the slope of the IA mass scaling, respectively. In our analysis, we incorporate the joint posterior on $A_{\rm IA}$ and β from Fortuna et al. (2025) as a prior, approximating it with a bivariate Gaussian distribution. Furthermore, we apply a multivariate Gaussian prior on the halo mass for each tomographic bin.

The cosmic shear measurements are combined with the DES Y3 data (Amon et al. 2022; Secco et al. 2022). As in Dark Energy Survey and Kilo-Degree Survey Collaboration (2023), roughly eight per cent of the DES data are removed to avoid overlap with KiDS. We do not use HSC Y3 data (Dalal et al. 2023; Li et al. 2023c); while the likelihood is publicly available, there is significant overlap between the surveys. Since the overall constraining power of HSC Y3 is weaker than the combined power of KiDS and DES, we do not expect this omission to change the results.

2.2. BAO and RSD data

We use BAO measurements (BAO scale, not including the Alcock-Paczyński effect) from DESI DR2 (Desi & Abdul-Karim 2025). DESI contains a bright galaxy survey (BGS, Hahn et al. 2023), luminous red galaxies (LRGs, Zhou et al. 2023), emission line galaxies (ELGs, Raichoor et al. 2023), the Lyman-α forest (du Mas des Bourboux et al. 2020), and quasars (QSOs, Chaussidon et al. 2023); cosmological BAO results are given in Adame et al. (2025). We employ the public DESI likelihood measurements for BGS ($z \in [0.1, 0.4)$), two LRG bins ($z \in [0.4, 0.6)$ and $z \in [0.6, 0.8)$, respectively), ELG ($z \in [1.1, 1.6)$), combined LRG+ELG ($z \in [0.8, 1.1)$, QSO ($z \in [0.8, 2.1)$) and Lyman-α forest ($z \in [1.77, 4.16)$) samples. From the RSD measurements of the growth rate, we use the following data: the Sloan Digital Sky Survey DR7 main galaxy sample (Ross et al. 2015; Howlett et al. 2015), BOSS DR12 (Alam et al. 2021), eBOSS DR16 ELGs (Tamone et al. 2020; Raichoor et al. 2023; de Mattia et al. 2021), eBOSS DR16 LRGs (Bautista et al. 2021; Gil-Marín et al. 2020), eBOSS DR16 QSOs (Neveux et al. 2020; Hou et al. 2021).

2.3. CMB data

We use CMB data from Planck Collaboration V (2020), employing the compressed Planck likelihood of Prince & Dunkley (2019) where the $\ell < 30$ temperature likelihood is approximated by two Gaussian points, and PLIK-LITE TTTEEE is used for $\ell > 30$. We impose a Gaussian prior on the reionisation optical depth τ, derived from Planck base ΛCDM constraints, to mimic the constraints from low-multipole polarisation measurements. We note that the low-multipole polarisation measurements are not directly sensitive to the extensions studied in this paper. However, as discussed, for example, in Sailer et al. (2026), a larger optical depth would reduce some of the discrepancy with low-redshift probes. The origin of this remains unclear. For the CMB lensing signal, we employ the Planck lensing signal from Carron et al. (2022). We do not vary the nuisance parameter $A_{\rm lens}$ in the fiducial analysis. This is motivated by the addition of CMB data where $A_{\rm lens}$ was found to be consistent with unity (Camphuis et al. 2025). For an extended discussion of the effect of $A_{\rm lens}$, we refer to our companion paper (Stölzner et al. 2026).

[5] To determine fractions, we use the template-fitting code BPZ (Benítez 2000), which provides T_B as an output.

Table 3. Bayes factors, B as defined in Eq. (2), for the extended models for the different probe combinations.

Probes	Bayes factor		
	w_0/Λ	w_0w_a/Λ	Ω_K/flat
KiDS	0.38	0.2	0.95
lensing	0.19	0.07	0.56
low-z	0.09	0.02	0.17
low-z+CMB	0.22	2.73	0.38

Notes. The columns always compare the extended model to the fiducial flat ΛCDM. This means that $B > 1$ prefers the extension, while $B < 1$ prefers flat ΛCDM. According to the Jeffreys' scale, there is no significant evidence for any of the extended models being preferred over the extensions tested here for any data combination. Even more so, extensions to flat ΛCDM are disfavoured in all but one case.

Furthermore, we add ACT DR6 lensing and primary CMB (Qu et al. 2024; Madhavacheril et al. 2024; Naess et al. 2025; Louis et al. 2025; Calabrese et al. 2025) combined with SPT-3G D1 temperature and polarisation anisotropies (Camphuis et al. 2025). The SPT lensing signal is taken from SPT-3G 2018 (Pan et al. 2023). For these datasets, we use the CANDL likelihood (Balkenhol et al. 2024). To remove correlations between ACT and Planck, the Planck data are used only for $\ell < 1000$ and $\ell < 600$ in TT and TEEE, respectively. The correlations between Planck + ACT and SPT are negligible, as SPT-3G D1 only covers a small portion of the sky. Although some cross-correlation is present in the CMB lensing signals, Qu et al. (2026) showed that it has a negligible impact on the reported error bars. We therefore append the ACT and SPT data to our data vector at multipoles larger than the limits above.

Lastly, we neglect any cross-correlation between the cosmic shear and CMB lensing signals in the covariance matrix. Robertson et al. (2021), Yao et al. (2023) measured the cross-correlation of KiDS-1000 with the CMB lensing signal of the Atacama Cosmology Telescope, and Omori et al. (2023) did the same for DES Y3, Planck, and SPT. Thus, although there is clear cross-correlation between the signals, the cross-covariance between the CMB and cosmic shear auto-correlation function will still be relatively small. The reason is that the auto-correlation covariance contains reconstruction noise and shape noise, in addition to the auto-correlation signal. For the cross-covariance, only the signal component of the cross-correlation is relevant, and it is smaller than the auto-correlation.

2.4. Supernova data

For the evolving dark energy models, we furthermore use measurements of Type Ia supernovae from the Pantheon+ compilation (Scolnic et al. 2022), consisting of 1701 light curves of 1550 spectroscopically confirmed SNIa with redshifts $z \in (0.001, 2.26)$. Inference of cosmological parameters from this dataset was presented in Brout et al. (2022).

2.5. Data combinations used

The data combinations used are summarised in Table 1. We focus on constraints from KiDS-Legacy alone, which we refer to as KiDS in the discussion and plots. The combination of SPT, Planck, and ACT is labelled CMB (this corresponds to the SPA likelihood in Camphuis et al. 2025). All probes that use the weak gravitational lensing effect, that is, CMB lensing, KiDS, and DES Y3, are collectively referred to as 'lensing'. We label the low-redshift probes as low-z, that is, those that do not depend on the CMB. Lastly, we combine all probes but the supernovae into the low-z+CMB likelihood. All external likelihoods used in this work are publicly available and implemented in the CosmoSIS standard library[6] (Zuntz et al. 2015).

2.6. Inference

We use CosmoPipe and sample the parameter space via the Nautilus[7] sampler (Lange 2023) to generate samples from the posterior distribution. As a nested sampling method (Skilling 2006), Nautilus allows for direct computation of the evidence and hence easy estimation of the Bayes factor B for model comparison:

$$B = \frac{p(D|M_1)}{p(D|M_2)}\,, \tag{2}$$

where $p(D|M_1)$ is the evidence of the model M_1. If $B > 1$, M_1 is preferred over model M_2 and vice versa for $B < 1$. The amount of preference can be quantified using the Jeffreys' scale. It quantifies a model preference with $|\log_{10} B| > [0.5, 1, 2]$ as 'substantial', 'strong', and 'decisive'. The Bayes ratio suffers from several shortcomings: it is prior-dependent, not a probability, and, as a result, the Jeffreys scale is somewhat arbitrary. To avoid prior effects, we also report the tension between the two models based on suspiciousness (Handley & Lemos 2019), where the parameter posteriors indicate some level of tension. For more details, we refer to Section 3.2.1 in Stölzner et al. (2025). However, since most models will be very consistent with the fiducial ΛCDM analysis, we will use the Bayes factors. For Nautilus, we use the following settings: $f_{\rm live} = 0.01$, $N_{\rm live} = 3000$, and $N_{\rm eff} = 10000$.

We use the cosmological parameter inference code CosmoSIS (Zuntz et al. 2015) to facilitate all of our computations and use CAMB (Lewis et al. 2000) for the corresponding linear power spectrum to be fed into HMCODE2020 for the non-linear power spectra. The likelihood for each probe is assumed to be a multivariate Gaussian likelihood with the cosmic shear covariance matrix calculated via the OneCovariance[8] (Reischke et al. 2025) at the ΛCDM best-fit cosmology.

A list of model parameters is provided in Table 2. For brevity, we show only nuisance parameters relevant to cosmic shear. The flat ΛCDM parameters are the reduced Hubble constant $h = H_0[\mathrm{km\,s^{-1}Mpc^{-1}}]/100$, the cold dark matter and baryon densities $\omega_{\rm cdm} = \Omega_{\rm cdm}h^2$ and $\omega_{\rm b} = \Omega_{\rm b}h^2$, the spectral index of the primordial power spectrum and its amplitude, which we parametrise by either the variance σ_8^2 in spheres of $8\,\mathrm{Mpc}/h$, or by the amplitude of the matter power spectrum $A_{\rm s}$ at a pivot scale $k = 0.05\,\mathrm{Mpc}^{-1}$. Since cosmic shear is most sensitive to $S_8 = \sigma_8\sqrt{\Omega_{\rm m}/0.3}$, we use S_8 by default as the sampling parameter and derive the others. For the extended models, we use the sum of the neutrino masses $\sum m_\nu$, the spatial curvature parameter defined in Eq. (5), and the w_0, w_a-parametrisation as in Eq. (3).

3. Constraints on extended models

In this section, we present the results for the extended cosmological models and for different combinations of datasets.

[6] https://github.com/cosmosis-developers/cosmosis-standard-library/tree/v4.0/likelihood
[7] https://github.com/johannesulf/nautilus
[8] https://github.com/rreischke/OneCovariance

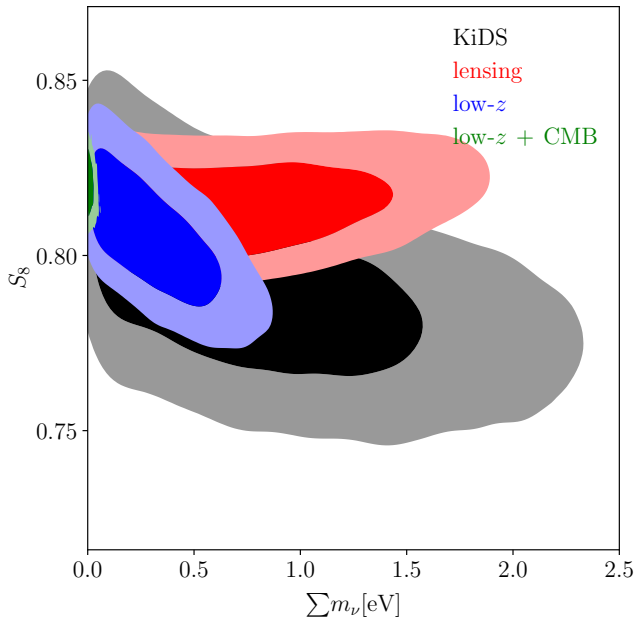

Fig. 1. Marginalised two-dimensional 68% and 95% credible regions in the S_8, $\sum m_\nu$ plane. Different colours represent the probe combinations discussed in Table 1.

For quick reference, the Bayes factors for model selection are shown in Table 3. The marginal mean and its corresponding 68% credible interval for all probe and model combinations for the main cosmological parameters are summarised in Table 4. We also show the p-values, calculated using the recipe discussed in Stölzner et al. (2025) (see Sect. 3.2.1), for the KiDS data alone for each case. This result differs slightly from Wright et al. (2025b), where the maximum a posteriori (MAP) probability was explicitly calculated: here, instead, we use the MAP from the posterior samples. As a result, the p-values presented here are an upper limit.

Here, we focus on the constraints on the parameters specific to the extended models studied and their interplay with S_8. For more details, we show the full contours for all cosmological parameters and the feedback parameter in Appendix B. We find that the nuisance parameters, in particular the intrinsic alignment parameters, as well as the redshift calibration parameters, are prior-dominated and exhibit no cross-talk with extended models and probes. More precisely, the extended model parameters do not exhibit strong degeneracies with the nuisance parameters in the range allowed by the priors and the overall signal-to-noise of the cosmic shear measurement. Lastly, we note that constraints on Ω_K and $\sum m_\nu$ from lensing alone are not competitive with those from the CMB or BAO, and in particular with their combination. However, the current comparison is not on equal footing, as cosmic shear is still in its golden years. Hence, this situation will improve as we move to Stage IV surveys (see Euclid Collaboration: Blanchard et al. 2020; Euclid Collaboration: Archidiacono et al. 2025), or forecasted constraints on curvature or neutrinos).

3.1. Neutrinos

The observation of neutrino oscillations necessitates that at least two of the three neutrino mass eigenstates have non-zero mass. Hence, their sum $\sum m_\nu > 0$. In what follows, we express the neutrino mass in natural units, that is, $c = 1$. In the fiducial KiDS analysis, $\sum m_\nu = 0.06\,\mathrm{eV}$ was assumed, which is in line with the lowest allowed mass range in the normal hierarchy from oscillation measurements (de Salas et al. 2021; Esteban et al. 2020, 2024). Other laboratory experiments can instead give upper limits, $\leq 0.45\,\mathrm{eV}$ (at 90%) via double-β decay (this is, though, a weighted sum of the neutrino masses with the weights given by the PMNS mixing matrix; Katrin & Aker 2025). Due to their low mass and resulting high thermal velocities, neutrinos do not cluster on small scales, thus suppressing the growth of structures (see e.g. Lesgourgues & Pastor 2006; Tereno et al. 2009; Abazajian et al. 2015; Gerbino & Lattanzi 2017, for overviews as well as first constraints with cosmic shear). Constraints from cosmology are mainly dominated by the CMB (Planck Collaboration VI 2020; Camphuis et al. 2025), limiting $\sum m_\nu < 0.17\,\mathrm{eV}$. In combination with BOSS (Ivanov et al. 2020) and DESI (Adame et al. 2025), the cosmological measurement of $\sum m_\nu$ approaches the lower bound set by oscillation experiments, assuming the normal hierarchy. Here, we investigate the influence of varying neutrino mass on the constraints on S_8 by KiDS as well as the upper limits on $\sum m_\nu$ themselves. In the analysis presented here, we assume the normal hierarchy. For consistency with many other analyses, we run CAMB (Lewis et al. 2000) with fixed $N_{\rm eff}$ and three neutrino species approximated as a single massive and two massless eigenstates (as in Planck Collaboration VI 2020) and pass their sum to HMCODE2020, a combination which was tested against HALOFIT in Camphuis et al. (2025) and found to give changes of 0.2σ. However, this implies the existence of two ultra-relativistic species. As a result, the inferred total neutrino mass tends to be systematically lower compared with the fully degenerate mass scenario (see e.g. Loureiro et al. 2019; Choudhury & Hannestad 2020).

Fig. 1 shows the marginalised constraints in the S_8, $\sum m_\nu$ plane for the different probe combinations listed in Table 1. Since neutrinos affect clustering directly but also change the background by reducing $\Omega_{\rm m}$ when increasing $\sum m_\nu$, the interpretation is less straightforward than, for example, for feedback. Interestingly, we find a small anti-correlation between S_8 and $\sum m_\nu$ for KiDS alone. More probability mass at larger neutrino masses shifts the peak of the matter power spectrum towards lower wave numbers, k, thereby favouring slightly larger values of the spectral index, $n_{\rm s}$. This overall shift results in a slight amplitude gain for the cosmic shear signal, which, in turn, is accompanied by a slightly lower value of S_8.

However, as this is not a significant shift in the parameters, the p-value at the MAP ($S_8 = 0.793$ with neutrinos marginalised and $S_8 = 0.812$ for the fiducial analysis) is equally good as the one for the ΛCDM case with a fixed neutrino mass. The upper limit on the neutrino mass from KiDS alone is

$$\sum m_\nu \leq 1.97\,\mathrm{eV} \quad \text{(KiDS at 95\%)}\,,$$

that is, 95% of the marginal posterior probability in $\sum m_\nu$ lies below this value. Adding DES and, crucially, CMB lensing breaks the degeneracy with S_8, as the CMB lensing signal is sensitive to larger scales. The low-redshift probes, in turn, mainly fix the matter density, thus not breaking the degeneracy. The strongest constraints come from the CMB, particularly when combined with DESI data, as increasing $\sum m_\nu$ increases the expansion rate at the time of CMB release. To keep the sound horizon consistent with the data, $\Omega_{\rm m}$ must increase. However, DESI's lower $\Omega_{\rm m}$ thus gives very tight constraints on the neutrino masses for which we find $\sum m_\nu \leq 0.048\,\mathrm{eV}$ (at 95%), consistent with Camphuis et al. (2025) and in tension with the neutrino oscillation measurements, $\sum m_\nu \geq 0.058\mathrm{eV}$ for the normal

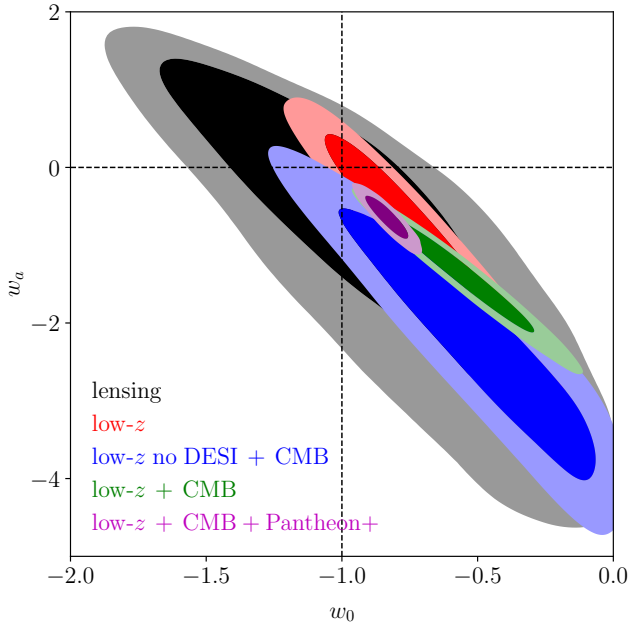

Fig. 2. Marginalised constraints on dynamical dark energy in the w_0, w_a parametrisation, Eq. (3). The black contour contains all cosmic shear probes considered in this work, and the red contour is independent of the CMB. The blue and green contours differ only in that the blue one excludes the DESI DR2 BAO. In purple, the Pantheon+ SN sample has been added. The dashed lines mark the ΛCDM values.

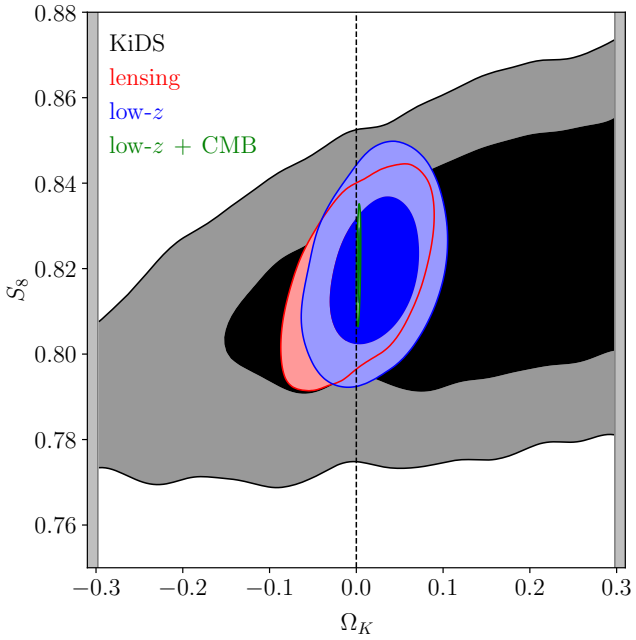

Fig. 3. Constraints on Ω_KCDM in the S_8, Ω_K plane. The colour scheme is the same as in Fig. 1. The low-z+CMB constraint (green) lies right next to the dashed line. The prior range is indicated by the grey bands.

hierarchy. In particular, these values appear to reject the normal hierarchy at 2.1σ and over 3σ for the inverted hierarchy. It is noteworthy that this value is also lower than the fiducial value in the KiDS-Legacy analysis. However, since this is a small change relative to the overall sensitivity of the cosmic shear data, it will not affect the results of that analysis.

As expected, the neutrino sector is not very well constrained with KiDS data alone, but constraints from cosmic shear alone are of similar quality compared to the previous KiDS-1000's $3\times$2pt analysis (Tröster et al. 2021).

3.2. Dark energy equation of state

We vary the dark energy equation of state parameter with the standard (CPL; Chevallier & Polarski 2001; Linder 2003) parametrisation:

$$w(a) = w_0 + w_a(1 - a), \tag{3}$$

with the uniform priors given in Table 2. We do not explicitly impose $w < -1/3$, which is required for accelerated expansion, in the prior. In this model, $w_0 = -1$ and $w_a = 0$ corresponds to the cosmological constant Λ. The cosmological background is modified so that:

$$E^2(a) = \Omega_{\rm m} a^{-3} + (1 - \Omega_{\rm m}) \exp\left(-3 \int_1^a {\rm d}a' \frac{1 + w(a')}{a'}\right), \tag{4}$$

where the spatial curvature still vanishes. This parametrisation has attracted considerable attention recently, owing to the DESI results, which have measured w_0 and w_a to be discrepant with Λ. This, in turn, has sparked a debate. For example, that the BAO data measures $w(z) = -1$ at the redshifts where the BAO has been measured (see e.g. Cortês & Liddle 2024; Efstathiou 2025), or whether prior volume effects play a role (e.g. Herold & Karwal 2025; Steinhardt et al. 2025; Bayat & Hertzberg 2025), if theoretical priors (e.g Lewis & Chamberlain 2025; Toomey et al. 2025; Caldwell & Linder 2025) can reconcile this tension, or if this hints towards non-minimally coupled gravity theories (Ye et al. 2025).

Here, we test the full w_0, w_a parametrisation and the subclass where $w_a = 0$, these are called w_0w_aCDM and wCDM respectively. For KiDS alone, we find the following constraints:

$$w_0 = -1.1^{+0.5}_{-0.5} \quad \text{(KiDS for } w_0\text{CDM at 68\%)},$$
$$w_0 = -1.0^{+0.7}_{-0.7} \quad \text{(KiDS for } w_0w_a\text{CDM at 68\%)},$$
$$w_a = -1.3^{+1.9}_{-2.0} \quad \text{(KiDS for } w_0w_a\text{CDM at 68\%)},$$

consistent with ΛCDM and thus the fiducial analysis of KiDS. The dark energy equation of state alters the expansion function and, consequently, the growth of structure. The constraints obtained from weak lensing on the equation of state are determined by the effective equation of state, $w_{\rm eff}$, at the mean redshift of the source distribution for each tomographic bin. Different models are then distinguished by the amount of structure growth from that point in time to today, and by what that point in time represents, that is, by the distance-redshift relationship. Increasing $w_{\rm eff}$ moves the source closer to the observer at fixed z, decreasing the lensing signal, requiring an increase in S_8. At the same time, however, the amount of structure growth at a given $z > 0$ is increased by increasing $w_{\rm eff}$ if the amplitude of the matter power spectrum is kept fixed. The exact degeneracy between S_8 and $w_{\rm eff}$ therefore depends on the redshift baseline of the survey in question and is difficult to disentangle since S_8 depends on $\Omega_{\rm m}$, which itself modifies the distance-redshift relation. Generally, however, one does find a strong positive correlation between S_8 and $w_{\rm eff}$. This is why weak lensing benefits significantly from the addition of external probes that fix either σ_8 or $\Omega_{\rm m}$.

In Fig. 2, we present the results for the w_0, w_a parametrisation with external probes, showing that the lensing and

Table 4. Marginal constraints for all probe combinations (compare Table 1) and models tested in this work.

Model	Probes	S_8	Ω_m	n_s	σ_8	$\log_{10} T_{AGN}$	$\sum m_\nu$ [eV]	w_0	w_a	Ω_K	p_{KiDS}
ΛCDM	KiDS	$\mathbf{0.813^{+0.018}_{-0.018}}$	$0.329^{+0.055}_{-0.054}$	$1.001^{+0.067}_{-0.070}$	$0.786^{+0.078}_{-0.079}$	$7.69^{+0.31}_{-0.29}$	0.06	-1	0	0	0.39
	Lensing	$\mathbf{0.8181^{+0.0094}_{-0.0098}}$	$\mathbf{0.281^{+0.016}_{-0.016}}$	$0.974^{+0.038}_{-0.041}$	$\mathbf{0.846^{+0.023}_{-0.024}}$	$7.54^{+0.19}_{-0.18}$	0.06	-1	0	0	0.43
	Low-z	$\mathbf{0.817^{+0.011}_{-0.010}}$	$\mathbf{0.2965^{+0.0081}_{-0.0079}}$	$1.035^{+0.043}_{-0.041}$	$\mathbf{0.824^{+0.016}_{-0.016}}$	$7.60^{+0.23}_{-0.22}$	0.06	-1	0	0	0.35
	Low-z+CMB	$\mathbf{0.8158^{+0.0061}_{-0.0056}}$	$\mathbf{0.3038^{+0.0031}_{-0.0029}}$	$\mathbf{0.9736^{+0.0032}_{-0.0031}}$	$\mathbf{0.8108^{+0.0033}_{-0.0041}}$	$7.50^{+0.15}_{-0.15}$	0.06	–1	0	0	0.38
$\nu\Lambda$CDM	KiDS	$\mathbf{0.79^{+0.02}_{-0.02}}$	$0.356^{+0.060}_{-0.061}$	$1.017^{+0.062}_{-0.065}$	$0.752^{+0.075}_{-0.075}$	$7.69^{+0.31}_{-0.29}$	$\mathbf{\leq 1.97}$	-1	0	0	0.49
	Lensing	$\mathbf{0.8149^{+0.0092}_{-0.0095}}$	$\mathbf{0.296^{+0.017}_{-0.018}}$	$0.981^{+0.043}_{-0.045}$	$\mathbf{0.821^{+0.024}_{-0.024}}$	$7.58^{+0.22}_{-0.21}$	$\mathbf{\leq 1.61}$	-1	0	0	0.39
	Low-z	$\mathbf{0.805^{+0.014}_{-0.014}}$	$\mathbf{0.2980^{+0.0077}_{-0.0083}}$	$1.050^{+0.037}_{-0.038}$	$\mathbf{0.818^{+0.017}_{-0.016}}$	$7.59^{+0.22}_{-0.22}$	$\mathbf{\leq 0.74}$	-1	0	0	0.39
	Low-z+CMB	$\mathbf{0.820^{+0.0059}_{-0.0057}}$	$\mathbf{0.3004^{+0.0029}_{-0.0030}}$	$\mathbf{0.9731^{+0.0031}_{-0.0031}}$	$\mathbf{0.8195^{+0.0048}_{-0.0047}}$	$7.51^{+0.16}_{-0.16}$	$\mathbf{\leq 0.048}$	–1	0	0	0.40
wCDM	KiDS	$\mathbf{0.809^{+0.040}_{-0.041}}$	$0.332^{+0.058}_{-0.059}$	$0.998^{+0.075}_{-0.080}$	$0.780^{+0.079}_{-0.078}$	$7.70^{+0.33}_{-0.30}$	0.06	$\mathbf{-1.10^{+0.45}_{-0.47}}$	0	0	0.39
	Lensing	$\mathbf{0.811^{+0.017}_{-0.016}}$	$\mathbf{0.268^{+0.039}_{-0.038}}$	$0.980^{+0.040}_{-0.042}$	$\mathbf{0.864^{+0.049}_{-0.048}}$	$7.54^{+0.19}_{-0.18}$	0.06	$\mathbf{-1.09^{+0.21}_{-0.21}}$	0	0	0.35
	Low-z	$\mathbf{0.824^{+0.013}_{-0.013}}$	$\mathbf{0.2970^{+0.0079}_{-0.0081}}$	$1.04^{+0.04}_{-0.04}$	$\mathbf{0.830^{+0.017}_{-0.017}}$	$7.60^{+0.23}_{-0.23}$	0.06	$\mathbf{-0.943^{+0.062}_{-0.064}}$	0	0	0.36
	Low-z+CMB	$\mathbf{0.8150^{+0.0052}_{-0.0063}}$	$\mathbf{0.2905^{+0.0069}_{-0.0067}}$	$\mathbf{0.972^{+0.003}_{-0.003}}$	$\mathbf{0.8284^{+0.0099}_{-0.0089}}$	$7.51^{+0.16}_{-0.16}$	0.06	$\mathbf{-1.06^{+0.03}_{-0.03}}$	0	0	0.32
w_0w_aCDM	KiDS	$\mathbf{0.799^{+0.041}_{-0.042}}$	$0.341^{+0.063}_{-0.063}$	$1.007^{+0.069}_{-0.075}$	$0.760^{+0.078}_{-0.078}$	$7.67^{+0.31}_{-0.27}$	0.06	$-0.98^{+0.65}_{-0.65}$	$\mathbf{-1.3^{+1.93}_{-2.01}}$	0	0.41
	Lensing	$\mathbf{0.815^{+0.020}_{-0.021}}$	$\mathbf{0.270^{+0.041}_{-0.040}}$	$0.984^{+0.041}_{-0.042}$	$\mathbf{0.864^{+0.047}_{-0.047}}$	$7.54^{+0.19}_{-0.18}$	0.06	$\mathbf{-0.92^{+0.45}_{-0.42}}$	$\mathbf{-0.88^{+1.45}_{-1.56}}$	0	0.41
	Low-z	$\mathbf{0.827^{+0.014}_{-0.013}}$	$\mathbf{0.322^{+0.026}_{-0.026}}$	$1.032^{+0.046}_{-0.044}$	$\mathbf{0.803^{+0.032}_{-0.032}}$	$7.61^{+0.24}_{-0.23}$	0.06	$\mathbf{-0.74^{+0.22}_{-0.21}}$	$\mathbf{-0.80^{+0.80}_{-0.83}}$	0	0.38
	Low-z+CMB	$\mathbf{0.8365^{+0.0084}_{-0.0076}}$	$\mathbf{0.329^{+0.013}_{-0.013}}$	$\mathbf{0.9709^{+0.0031}_{-0.0032}}$	$\mathbf{0.799^{+0.011}_{-0.011}}$	$7.53^{+0.18}_{-0.17}$	0.06	$\mathbf{-0.63^{+0.13}_{-0.13}}$	$\mathbf{-1.20^{+0.39}_{-0.38}}$	0	0.28
	Low-z+SPA+Pantheon+	$\mathbf{0.8270^{+0.0063}_{-0.0068}}$	$\mathbf{0.3101^{+0.0052}_{-0.0056}}$	$\mathbf{0.9713^{+0.0032}_{-0.0031}}$	$\mathbf{0.8135^{+0.0073}_{-0.0073}}$	$7.52^{+0.17}_{-0.17}$	0.06	$\mathbf{-0.831^{+0.052}_{-0.053}}$	$\mathbf{-0.65^{+0.19}_{-0.18}}$	0	0.32
	Low-z no DESI+CMB	$\mathbf{0.829^{+0.013}_{-0.012}}$	$\mathbf{0.302^{+0.027}_{-0.027}}$	$\mathbf{0.9709^{+0.0032}_{-0.0033}}$	$\mathbf{0.828^{+0.025}_{-0.025}}$	$7.51^{+0.16}_{-0.16}$	0.06	$\mathbf{-0.51^{+0.32}_{-0.31}}$	$\mathbf{-2.26^{+1.15}_{-1.12}}$	0	0.38
$\Omega_K\Lambda$CDM	KiDS	$\mathbf{0.816^{+0.021}_{-0.021}}$	$0.336^{+0.058}_{-0.057}$	$0.994^{+0.073}_{-0.075}$	$0.782^{+0.080}_{-0.079}$	$7.72^{+0.33}_{-0.30}$	0.06	-1	0	$0.08^{+0.16}_{-0.17}$	0.48
	Lensing	$\mathbf{0.818^{+0.010}_{-0.011}}$	$\mathbf{0.282^{+0.018}_{-0.018}}$	$0.97^{+0.07}_{-0.07}$	$\mathbf{0.85^{+0.03}_{-0.03}}$	$7.55^{+0.20}_{-0.19}$	0.06	-1	0	$\mathbf{0.001^{+0.040}_{-0.041}}$	0.34
	Low-z	$\mathbf{0.820^{+0.011}_{-0.011}}$	$\mathbf{0.2932^{+0.0096}_{-0.0097}}$	$1.040^{+0.041}_{-0.041}$	$\mathbf{0.832^{+0.019}_{-0.019}}$	$7.60^{+0.23}_{-0.22}$	0.06	-1	0	$\mathbf{0.022^{+0.034}_{-0.034}}$	0.43
	Low-z+CMB	$\mathbf{0.8208^{+0.0061}_{-0.0052}}$	$\mathbf{0.3032^{+0.0027}_{-0.0028}}$	$\mathbf{0.9695^{+0.0035}_{-0.0036}}$	$\mathbf{0.8165^{+0.0042}_{-0.0045}}$	$7.52^{+0.17}_{-0.17}$	0.06	-1	0	$\mathbf{0.0026^{+0.001}_{-0.001}}$	0.32

Notes. The constraints are provided as the marginal mean and the 68% confidence interval relative to it. For neutrinos, we quote the 95% upper limit. The last column shows the p-values (calculated as the probability-to-exceed) at the maximum a posteriori (MAP) for KiDS in the specific data and model combination. Numbers shown in bold are parameters which are constrained by the given model and probe combination (see Appendix A in Asgari et al. 2021). We note that, because parameters such as $\log_{10} T_{AGN}$ have highly asymmetric posterior distributions, we do not report a mode. Lastly, the constraints on h are not explicitly given, as we focus on those parameters potentially constrained by current lensing data.

low-z probe combinations are consistent with ΛCDM. The addition of CMB data to the low-redshift probes (green contours) moves the best fit away from ΛCDM, since the CMB is able to break degeneracies in the DESI data with Ω_m, making the low-z+CMB combination particularly strong. Crucially, as the green contour, although shifted away slightly from a cosmological constant, is consistent with ΛCDM, the addition of BAO data as measured by DESI is extremely important to move the contours away from ΛCDM. We remark that the prior range on h (see Table 2) is fairly tight. This choice is based on the ΛCDM analysis of KiDS-Legacy (Wright et al. 2025b). It does not restrict the analysis in ΛCDM when combining with the CMB (Stölzner et al. 2025). However, opening the parameter space for dynamical dark energy leads to a large posterior probability at low values of h and high values of Ω_m, as can be seen in Fig. B.1d. This occurs since the CMB is mostly sensitive to the physical density $\rho_m \sim h^2\Omega_m$. Hence, when performing an analysis that includes SPA, we increase the prior range for h. In turn, this changes the Bayes factor as it depends on the prior volume, again motivating reporting the suspiciousness as well.

Since the lensing probes are consistent with ΛCDM and provide an excellent fit with a p-value of 0.3, the Bayes factor, B in Eq. (2), that is the evidence of the w_0w_aCDM model over the evidence of ΛCDM given the same data, clearly prefers a cosmological constant over dynamical dark energy with $B = 0.07$. It is noteworthy that this is a stronger preference for ΛCDM than the Bayes factor suggests for the low-z+CMB combination, for which we find $B = 2.73$ in favour of w_0w_aCDM. Especially adding SN from Pantheon+ removes the lower part of the posterior and moves it closer to ΛCDM; the preference for dynamical dark energy becomes smaller in this case. In terms of suspiciousness, we find tensions of 2.6σ and 0.4σ with respect to ΛCDM for the low-z+CMB and lensing, respectively. The 2.6σ suspiciousness tension is not the same as the 2.6σ difference of Ω_K from zero. The former is related to the Bayes factor, while the latter is a significance in the posterior space. In fact, those significances for w_0 and w_a are 3.25σ and 3.4σ, respectively. Furthermore, we investigate the tension between our lensing dataset and the CMB+BAO. We use the Monte Carlo parameter-shift method introduced by Raveri et al. (2020) and find a tension of 0.5σ in the w_0, w_a plane, driven by the larger uncertainties for dynamical dark energy when using the lensing data. In general, we do not find any shifts larger than 2σ with this method.

3.3. Spatial curvature

In a universe with spatial curvature, the (comoving) angular diameter distance changes from being equal to the comoving distance, χ, to

$$f_K(\chi) = \begin{cases} K^{-1/2}\sin(K^{1/2}\chi) & \text{for } K > 0 \\ \chi & \text{for } K = 0 \\ |K|^{-1/2}\sinh(|K|^{1/2}\chi) & \text{for } K < 0 \end{cases} . \tag{5}$$

Due to the closure equation, the Hubble function is modified as

$$E(a) \coloneqq \frac{H(a)}{H_0} = \sqrt{\Omega_m a^{-3} + (1 - \Omega_m - \Omega_K) + \Omega_K a^{-2}}, \tag{6}$$

where $\Omega_K = -(c/H_0)^2 K$ is the spatial curvature parameter. Lastly, we assume that the modified structure formation in a spatially curved universe is entirely dictated by the linear power spectrum, while non-linear corrections are implicitly accounted for via the background. Terasawa et al. (2022) discuss the effect

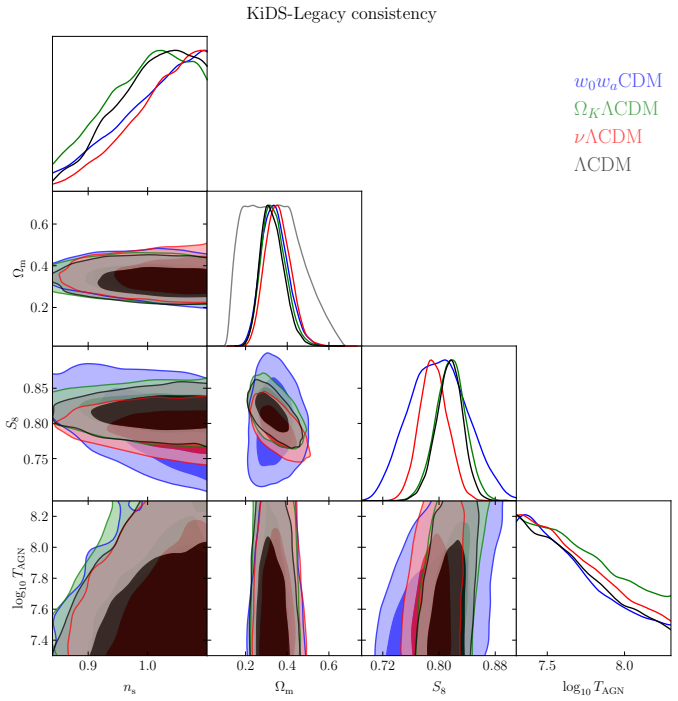

Fig. 4. Constraints on ΛCDM parameters from KiDS-Legacy alone when opening up the parameter space. The grey line in the marginalised Ω_m indicates the prior range. All other parameters have hard priors as shown.

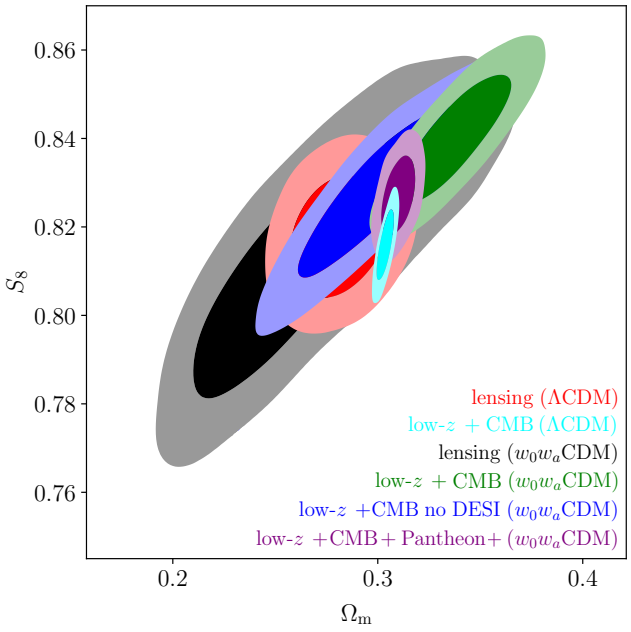

Fig. 5. Constraints on Ω_m and S_8 for different data combinations in the w_0, w_a parametrisation, Eq. (3). The red and the cyan contours assume a ΛCDM prior.

of $\Omega_K \neq 0$ on the non-linear power spectrum using a separate universe approach and the halo model. The leading-order terms are captured via the linear growth in our approach, while higher-order terms are neglected. Hence, the results presented here can be seen as conservative.

The CMB (e.g. Planck Collaboration VI 2020; Camphuis et al. 2025) yields strong constraints on Ω_K via the position of the first acoustic peak in the CMB angular power spectrum. Due to its degeneracy with the matter density, a combination with BAO data tightens constraints significantly, providing $\Omega_K = (0.26 \pm 0.11) \times 10^{-2}$ roughly 2σ away from spatial flatness.

Fig. 3 displays the constraints on Ω_K together with S_8 from KiDS, lensing, low-z, and all considered probes in black, red, blue, and green, respectively. The dashed line indicates a spatially flat universe, and Ω_K is shown over the whole prior range. One can see that KiDS alone provides only mild constraints on Ω_K, as it lies within the prior edge for $\Omega_K > 0$ and within the prior edge for $\Omega_K < 0$. This is expected, as measuring spatial curvature requires a meaningful observation of absolute physical scales, which lensing struggles to provide. Alternatively, adding CMB lensing already increases the constraining power substantially, as it provides measurements on larger scales and can therefore resolve the peak of the matter power spectrum, providing constraints on Ω_m and hence Ω_K, yielding

$$\Omega_K = 0.00 \pm 0.04 \quad \text{(lensing for } \Omega_K\Lambda\text{CDM at 68\%)}.$$

Adding BAO to cosmic shear provides similar constraints, again via breaking the Ω_m degeneracy. The influence of the constraints on S_8 is negligible. Adding the CMB recovers the constraints provided in Camphuis et al. (2025) due to the high signal-to-noise ratio of the acoustic peak position.

3.4. Consistency of KiDS-Legacy

Stölzner et al. (2025) provided several internal consistency checks of the KiDS-Legacy dataset. Here, we also summarise the consistency when adding more datasets and expanding the parameter space.

First, Fig. 4 shows the constraints for Ω_m, the spectral index n_s and S_8 for the three extended models studied here in comparison to the fiducial analysis from Wright et al. (2025b). It can be seen that the modes of the posterior marginals are very stable, with the largest shift occurring in S_8 when varying the neutrino mass, as discussed already before. Furthermore, the constraints on S_8 degrade when dynamical dark energy is included. This is because a more negative $w_{\rm eff}$ moves sources further away at a given redshift, requiring less matter clustering, leading to a positive correlation between $w_{\rm eff}$ and S_8. We also measure the Kullback-Leibler divergence, $D_{\rm KL}$, between marginal posterior distributions p_1 and p_2, that is their relative entropy:

$$D_{\rm KL}(p_1, p_2) = \int \mathrm{d}x\, p_1(x) \log \frac{p_1(x)}{p_2(x)}\,. \tag{7}$$

The largest Kullback-Leibler divergence in S_8 is $D_{\rm KL} = 0.45$ in the case of the neutrinos, a shift of 1.2σ of the marginal mean relative to the fiducial analysis.

In Fig. 5, we show the consistency of different probe combinations in the Ω_m, S_8 plane and how dynamical dark energy moves these specific contours. One can see the shift to higher Ω_m and hence S_8 when adding the DESI results to the low-redshift and the CMB data (from the blue to the green contour). This shift, however, is reduced when adding in the SN from Pantheon+, bringing Ω_m down again. This does not mean that the tension with Λ is reduced, as only the negative w_a tail of the posterior is removed. While this moves the peak of the posterior closer to ΛCDM, the overall discrepancy with it stays the same (as was shown in Fig. 2). We observe the same shift for this data combination when moving from ΛCDM to w_0w_aCDM (from the cyan to the purple contour). It is only in these

scenarios where SN observations add constraining power. While we do not show it explicitly, low-z+SPA+Pantheon+ in ΛCDM agrees with low-z+SPA. Lastly, we show the effect on the lensing probes (from the black contour to the red contour) when using the w_0, w_a parametrisation, which is consistent with the fiducial analysis.

Fig. 6 displays a summary of the main probe and model combinations tested in this work. We show the marginal mean, together with the 68% confidence interval, of the main parameter constrained by cosmic shear, S_8, for each combination, and highlight the fiducial ΛCDM analyses by KiDS-Legacy and Planck in blue and grey, respectively. Additionally, we present the case in which we keep w_a fixed at zero and only vary w_0, referred to as wCDM. We observe that the marginal constraints on S_8 remain stable as the parameter space is expanded or additional probes are included. In ΛCDM, we find S_8 to be unchanged and a per cent measurement from lensing alone, which turns into a sub-per cent measurement when combining all probes considered here. The shift in S_8 when varying the neutrino mass reduces when including external data, as expected, as the combination of CMB and BAO pushes the neutrino mass very close to the value used in the fiducial analysis.

For dynamical dark energy, wCDM does not affect the marginal mean of S_8 strongly and simply increases the error bars. This is consistent with the fact that BAO and the CMB agree at $w_0 = -1$ when w_a is held fixed. However, when considering the full w_0, w_a parametrisation, the combination of all probes actually prefers high S_8. The shift is mainly driven by an increasing Ω_m, while σ_8 does change less. This can, again, be quantified by the Kullback-Leibler divergence for which we find $D_\mathrm{KL} = 3$ (2.3σ) for S_8 but $D_\mathrm{KL} = 1.4$ (1.1σ) for σ_8. Interestingly, the value of σ_8 is lowered in the dynamical dark energy scenario. However, as previously discussed, the preference for this extended model is relatively small.

As indicated in Table 4, some of the parameters are not constrained by the likelihood but rather via our prior choice; this is most pronounced for $\log_{10} T_\mathrm{AGN}$. Consequently, those posteriors have very non-Gaussian distributions, which can lead to projection effects. The main parameter of interest in the previous discussion, however, is S_8 whose interplay with $\log_{10} T_\mathrm{AGN}$ is studied in Appendix A. Since we do not find significant changes in S_8 due to $\log_{10} T_\mathrm{AGN}$, we conclude that projection effects are not dominant.

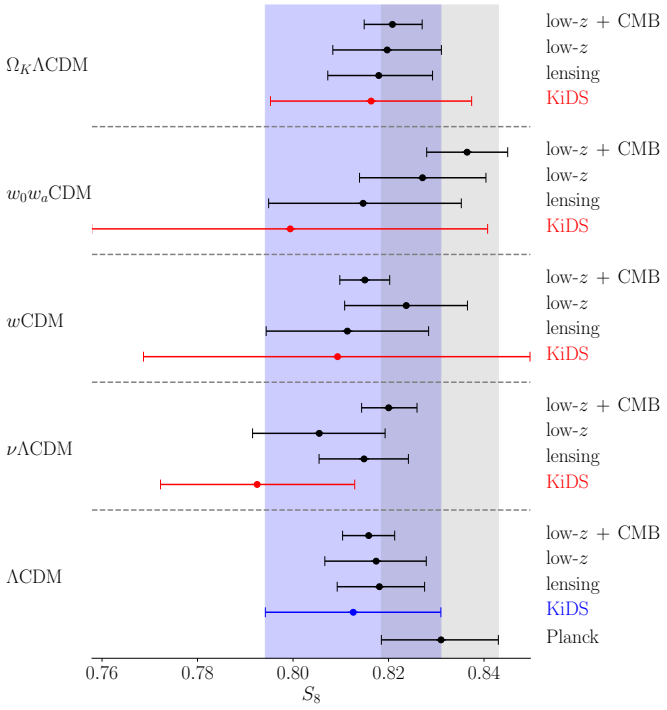

Fig. 6. Marginal mean of S_8 and the 68% credible interval for all extended models and probe combinations tested in this work. The blue band shows the ΛCDM constraints from KiDS (Wright et al. 2025b), while the grey band shows the constraints from Planck (Planck Collaboration VI 2020).

4. Summary

We present the extended cosmology analysis of the final cosmic shear catalogue of the Kilo-Degree Survey (KiDS-Legacy) in combination with external cosmic shear data from the Dark Energy Survey (DES), as well as external probes from the cosmic microwave background (CMB), baryon acoustic oscillations (BAOs), and redshift space distortion (RSD). Due to the consistency of KiDS-Legacy with other cosmological probes, especially in $S_8 = \sigma_8 \sqrt{\Omega_\mathrm{m}/0.3}$, we can, for the first time, reliably combine with all external datasets. We derive constraints on the sum of neutrino masses, the spatial curvature of the Universe, and the equation of state of dark energy. Furthermore, we investigate the robustness of the KiDS-Legacy data to different combinations of data and parameter space extensions.

We find that KiDS-Legacy prefers ΛCDM over extended models, with almost identical goodness of fit across all extended models considered, and that the Bayes factors are all below unity, disfavouring extended models. By combining KiDS-Legacy with DES Y3 and CMB lensing data from Planck, the Atacama Cosmology Telescope (ACT) and the South Pole Telescope (SPT), we define a lensing probe which enhances the consistency with ΛCDM, rejecting extended models according to the Jeffreys scale, especially time-evolving dark energy models, with a Bayes factor $B < 1$. The equation of state of these models is constrained to $w_0 = -0.92^{+0.45}_{-0.42}$ and $w_a = -0.88^{+1.45}_{-1.56}$ from weak gravitational lensing alone. Curvature and neutrinos are only poorly constrained by weak gravitational lensing with $\Omega_K = 0.001^{+0.040}_{-0.041}$ and $\sum m_\nu \leq 1.61\,\mathrm{eV}$.

Adding clustering data from BAOs and RSD significantly improves constraints compared to those from weak gravitational lensing alone, as Ω_m becomes tightly constrained, thereby breaking one of the main lensing degeneracies and allowing it to measure the amplitude of the linear matter power spectrum, σ_8. This low-redshift, low-z probe collection is independent of the CMB and is, to a substantial degree, consistent with ΛCDM, with all constraints consistent with ΛCDM within 1σ, and hence all Bayes factors disfavour the extended models.

When combining low-redshift data with CMB primary anisotropies and CMB lensing, we recover constraints on the neutrino mass and curvature from the CMB alone, which are much more sensitive to these parameters. For dynamical dark energy, however, the different preferences for Ω_m between the CMB and low-z probes shift $w(a)$ away from ΛCDM by roughly 3σ if allowed to vary with redshift. This, however, is less strong in terms of model selection than the preference of lensing probes for ΛCDM. More quantitatively, the Bayes factor, B is 0.07 (0.02) using our lensing (low-z) probes in preference of w_0w_aCDM over ΛCDM, thus corresponding to strong (very strong) evidence in favour of ΛCDM. In contrast, when combining all probes, we only find $B = 2.73$.

The cosmic shear analysis of KiDS-Legacy is robust to minimal extensions of ΛCDM, preferring it over all other models

while maintaining statistically stable inferred values of S_8 when the parameter space is expanded, or external probes are added. This extends the fiducial analysis of KiDS-Legacy naturally, while arriving at a similar conclusion: at the end of cosmic shear Stage-III surveys, cosmological probes, spanning 13 billion years, are strongly in favour of ΛCDM. With the tentative evidence for dynamical dark energy in DESI, cosmic shear is set to move to Stage-IV as well, providing much tighter constraints and decisively measuring $w(z)$.

Acknowledgements. The authors would like to thank L. Balkenhol, E. Camphuis, and S. Galli for their help and for pointing us to the right places for constructing the CMB likelihood. RR, AD, HHi, and CM are supported by a European Research Council Consolidator Grant (No. 770935). AHW is supported by the Deutsches Zentrum für Luft- und Raumfahrt (DLR), under project 50QE2305, made possible by the Bundesministerium für Wirtschaft und Klimaschutz, and acknowledges funding from the German Science Foundation DFG, via the Collaborative Research Center SFB1491 "Cosmic Interacting Matters - From Source to Signal". BS, and ZY acknowledge support from the Max Planck Society and the Alexander von Humboldt Foundation in the framework of the Max Planck-Humboldt Research Award endowed by the Federal Ministry of Education and Research. HHi is supported by a DFG Heisenberg grant (Hi 1495/5-1), the DFG Collaborative Research Centre SFB1491, and the DLR project 50QE2305. BJ acknowledges support from the ERC-selected UKRI Frontier Research Grant EP/Y03015X/1 and by STFC Consolidated Grant ST/V000780/1. MA is supported by the UK Science and Technology Facilities Council (STFC) under grant number ST/Y002652/1 and the Royal Society under grant numbers RGSR2222268 and ICAR1231094. LM acknowledges the financial contribution from the PRIN-MUR 2022 20227RNLY3 grant "The concordance cosmological model: stress-tests with galaxy clusters" supported by Next Generation EU and from the grant ASI n. 2024-10-HH.0 "Attività scientifiche per la missione Euclid – fase E". AL acknowledges support from the Swedish National Space Agency (Rymdstyrelsen) under Career Grant Project Dnr 2024-00171. MvWK acknowledges the support by UK STFC (grant no. ST/X001075/1), the UK Space Agency (grant no. ST/X001997/1), and InnovateUK (grant no. TS/Y014693/1). MB is supported by the Polish National Science Center through grant no. 2020/38/E/ST9/00395. JHD acknowledges support from an STFC Ernest Rutherford Fellowship (project reference ST/S004858/1). BG acknowledges support from the UKRI Stephen Hawking Fellowship (grant reference EP/Y017137/1). CH acknowledges support from the Max Planck Society and the Alexander von Humboldt Foundation in the framework of the Max Planck-Humboldt Research Award endowed by the Federal Ministry of Education and Research, and the UK Science and Technology Facilities Council (STFC) under grant ST/V000594/1. CG is funded by the MICINN project PID2022-141079NB-C32. IFAE is partially funded by the CERCA program of the Generalitat de Catalunya. SJ acknowledges the Dennis Sciama Fellowship at the University of Portsmouth and the Ramón y Cajal Fellowship from the Spanish Ministry of Science. KK acknowledges support from the Royal Society and Imperial College. LL is supported by the Austrian Science Fund (FWF) [ESP 357-N]. CM acknowledges support under the grant number PID2021-128338NB-I00 from the Spanish Ministry of Science. NRN acknowledges financial support from the National Science Foundation of China, Research Fund for Excellent International Scholars (grant n. 12150710511), and from the research grant from China Manned Space Project n. CMS-CSST-2021-A01. TT acknowledges funding from the Swiss National Science Foundation under the Ambizione project PZ00P2_193352 MY, SSL and HHo acknowledge funding from the European Research Council (ERC) under the European Union's Horizon 2020 research and innovation program (Grant agreement No. 101053992). *Software:* The figures in this work were created with MATPLOTLIB (Hunter 2007), making use of the NUMPY (Harris et al. 2020), SCIPY (Virtanen et al. 2020), COSMOPOWER (Spurio Mancini et al. 2022) and GETDIST (Lewis 2025) software packages. *Kilo-Degree Survey:* Based on observations made with ESO Telescopes at the La Silla Paranal Observatory under programme IDs 179.A-2004, 177.A-3016, 177.A-3017, 177.A-3018, 298.A-5015. *Dark Energy Spectroscopic Instrument:* This research used data obtained with the Dark Energy Spectroscopic Instrument (DESI). DESI construction and operations are managed by the Lawrence Berkeley National Laboratory. This material is based upon work supported by the U.S. Department of Energy, Office of Science, Office of High-Energy Physics, under Contract No. DE–AC02–05CH11231, and by the National Energy Research Scientific Computing Centre, a DOE Office of Science User Facility under the same contract. Additional support for DESI was provided by the U.S. National Science Foundation (NSF), Division of Astronomical Sciences under Contract No. AST-0950945 to the NSF's National Optical-Infrared Astronomy Research Laboratory; the Science and Technology Facilities Council of the United Kingdom; the Gordon and Betty Moore Foundation; the Heising-Simons Foundation; the French Alternative Energies and Atomic Energy Commission (CEA); the National Council of Science and Technology of Mexico (CONACYT); the Ministry of Science and Innovation of Spain (MICINN), and by the DESI Member Institutions: www.desi.lbl.gov/collaborating-institutions. The DESI collaboration is honoured to be permitted to conduct scientific research on Iolkam Du'ag (Kitt Peak), a mountain with particular significance to the Tohono O'odham Nation. Any opinions, findings, and conclusions or recommendations expressed in this material are those of the author(s) and do not necessarily reflect the views of the U.S. National Science Foundation, the U.S. Department of Energy, or any of the listed funding agencies. *SDSS-IV:* Funding for the Sloan Digital Sky Survey IV has been provided by the Alfred P. Sloan Foundation, the U.S. Department of Energy Office of Science, and the Participating Institutions. SDSS-IV acknowledges support and resources from the Center for High Performance Computing at the University of Utah. The SDSS website is www.sdss4.org. SDSS-IV is managed by the Astrophysical Research Consortium for the Participating Institutions of the SDSS Collaboration, including the Brazilian Participation Group, the Carnegie Institution for Science, Carnegie Mellon University, Centre for Astrophysics|Harvard & Smithsonian, the Chilean Participation Group, the French Participation Group, Instituto de Astrofísica de Canarias, The Johns Hopkins University, Kavli Institute for the Physics and Mathematics of the Universe (IPMU)/University of Tokyo, the Korean Participation Group, Lawrence Berkeley National Laboratory, Leibniz Institut für Astrophysik Potsdam (AIP), Max-Planck-Institut für Astronomie (MPIA Heidelberg), Max-Planck-Institut für Astrophysik (MPA Garching), Max-Planck-Institut für Extraterrestrische Physik (MPE), National Astronomical Observatories of China, New Mexico State University, New York University, University of Notre Dame, Observatário Nacional/MCTI, The Ohio State University, Pennsylvania State University, Shanghai Astronomical Observatory, United Kingdom Participation Group, Universidad Nacional Autónoma de México, University of Arizona, University of Colorado Boulder, University of Oxford, University of Portsmouth, University of Utah, University of Virginia, University of Washington, University of Wisconsin, Vanderbilt University, and Yale University. *Dark Energy Survey:* This project used public archival data from the Dark Energy Survey (DES). Funding for the DES Projects has been provided by the U.S. Department of Energy, the U.S. National Science Foundation, the Ministry of Science and Education of Spain, the Science and Technology FacilitiesCouncil of the United Kingdom, the Higher Education Funding Council for England, the National Center for Supercomputing Applications at the University of Illinois at Urbana-Champaign, the Kavli Institute of Cosmological Physics at the University of Chicago, the Center for Cosmology and Astro-Particle Physics at the Ohio State University, the Mitchell Institute for Fundamental Physics and Astronomy at Texas A&M University, Financiadora de Estudos e Projetos, Fundação Carlos Chagas Filho de Amparo à Pesquisa do Estado do Rio de Janeiro, Conselho Nacional de Desenvolvimento Científico e Tecnológico and the Ministério da Ciência, Tecnologia e Inovação, the Deutsche Forschungsgemeinschaft, and the Collaborating Institutions in the Dark Energy Survey. The Collaborating Institutions are Argonne National Laboratory, the University of California at Santa Cruz, the University of Cambridge, Centro de Investigaciones Energéticas, Medioambientales y Tecnológicas-Madrid, the University of Chicago, University College London, the DES-Brazil Consortium, the University of Edinburgh, the Eidgenössische Technische Hochschule (ETH) Zürich, Fermi National Accelerator Laboratory, the University of Illinois at Urbana-Champaign, the Institut de Ciències de l'Espai (IEEC/CSIC), the Institut de Física d'Altes Energies, Lawrence Berkeley National Laboratory, the Ludwig-Maximilians Universität München and the associated Excellence Cluster Universe, the University of Michigan, the National Optical Astronomy Observatory, the University of Nottingham, The Ohio State University, the OzDES Membership Consortium, the University of Pennsylvania, the University of Portsmouth, SLAC National Accelerator Laboratory, Stanford University, the University of Sussex, and Texas A&M University. Based in part on observations at Cerro Tololo Inter-American Observatory, National Optical Astronomy Observatory, which is operated by the Association of Universities for Research in Astronomy (AURA) under a cooperative agreement with the National Science Foundation. *Planck:* Based on observations obtained with Planck (http://www.esa.int/Planck), an ESA science mission with instruments and contributions directly funded by ESA Member States, NASA, and Canada. *SPT:* Supported by the National Science Foundation (NSF) through awards OPP-1852617 and OPP-2332483. Partial support is also provided by the Kavli Institute of Cosmological Physics at the University of Chicago. Argonne National Laboratory's work was supported by the U.S. Department of Energy, Office of High Energy Physics, under contract DE-AC02-06CH11357. *ACT*: Support for ACT was through the U.S. National Science Foundation through awards AST-0408698, AST- 0965625, and AST-1440226 for the ACT project, as well as awards PHY-0355328, PHY-0855887 and PHY- 1214379. Funding was also provided by Princeton University, the University of Pennsylvania, and a Canada Foundation for Innovation (CFI) award to UBC. ACT operated in the Parque Astronómico Atacama in northern Chile under the auspices of the Agencia Nacional de Investigación y Desarrollo (ANID). *Author contributions*: All

authors contributed to the development and writing of this paper. The authorship list is given in three groups: the lead authors (RR, BS, BJ) followed by two alphabetical groups. The first alphabetical group includes those who are key contributors to both the scientific analysis and the data products. The second group covers those who have either made a significant contribution to the data products or to the scientific analysis.

References

Abazajian, K. N., Arnold, K., Austermann, J., et al. 2015, Astropart. Phys., 63, 66
Adame, A. G., Aguilar, J., Ahlen, S., et al. 2025, JCAP, 2025, 021
Alam, S., Aubert, M., Avila, S., et al. 2021, Phys. Rev. D, 103, 083533
Amon, A., Gruen, D., Troxel, M. A., et al. 2022, Phys. Rev. D, 105, 023514
Asgari, M., Schneider, P., & Simon, P. 2012, A&A, 542, A122
Asgari, M., Lin, C.-A., Joachimi, B., et al. 2021, A&A, 645, A104
Bacon, D. J., Refregier, A. R., & Ellis, R. S. 2000, MNRAS, 318, 625
Balkenhol, L., Trendafilova, C., Benabed, K., & Galli, S. 2024, A&A, 686, A10
Bautista, J. E., Paviot, R., Vargas Magaña, M., et al. 2021, MNRAS, 500, 736
Bayat, Z., & Hertzberg, M. P. 2025, JCAP, 2025, 065
Benítez, N. 2000, ApJ, 536, 571
Bigwood, L., Amon, A., Schneider, A., et al. 2024, MNRAS, 534, 655
Brout, D., Scolnic, D., Popovic, B., et al. 2022, ApJ, 938, 110
Broxterman, J. C., Simon, P., Porth, L., et al. 2025, A&A, 703, L3
Calabrese, E., Hill, J. C., Jense, H. T., et al. 2025, JCAP, 2025, 063
Caldwell, R. R., & Linder, E. V. 2025, ArXiv e-prints [arXiv:2511.07526]
Camphuis, E., Quan, W., Balkenhol, L., et al. 2025, ArXiv e-prints [arXiv:2506.20707]
Carron, J., Mirmelstein, M., & Lewis, A. 2022, JCAP, 2022, 039
Chaussidon, E., Yèche, C., Palanque-Delabrouille, N., et al. 2023, ApJ, 944, 107
Chevallier, M., & Polarski, D. 2001, Int. J. Mod. Phys. D, 10, 213
Choudhury, S. R., & Hannestad, S. 2020, JCAP, 2020, 037
Cortês, M., & Liddle, A. R. 2024, JCAP, 2024, 007
Dalal, R., Li, X., Nicola, A., et al. 2023, Phys. Rev. D, 108, 123519
Dark Energy Survey and Kilo-Degree Survey Collaboration (Abbott, T. M. C., et al.) 2023, OJA, 6, 36
de Jong, J. T. A., Verdoes Kleijn, G. A., Kuijken, K. H., & Valentijn, E. A. 2013, Exp. Astron., 35, 25
de Mattia, A., Ruhlmann-Kleider, V., Raichoor, A., et al. 2021, MNRAS, 501, 5616
de Salas, P. F., Forero, D. V., Gariazzo, S., et al. 2021, JHEP, 2021, 71
Desi, C., Abdul-Karim, M., et al. 2025, Phys. Rev. D, 112, 083515
Di Valentino, E., Said, J. L., Riess, A., et al. 2025, Phys. Dark Univ., 49, 101965
du Mas des Bourboux, H., Rich, J., Font-Ribera, A., et al. 2020, ApJ, 901, 153
Edge, A., Sutherland, W., Kuijken, K., et al. 2013, The Messenger, 154, 32
Efstathiou, G. 2025, MNRAS, 540, 2844
Esteban, I., Gonzalez-Garcia, M. C., Maltoni, M., Schwetz, T., & Zhou, A. 2020, JHEP, 2020, 178
Esteban, I., Gonzalez-Garcia, M. C., Maltoni, M., et al. 2024, J. High Energy Phys., 2024, 216
Euclid Collaboration (Blanchard, A., et al.) 2020, A&A, 642, A191
Euclid Collaboration (Archidiacono, M., et al.) 2025, A&A, 693, A58
Fenech Conti, I., Herbonnet, R., Hoekstra, H., et al. 2017, MNRAS, 467, 1627
Fortuna, M. C., Dvornik, A., Hoekstra, H., et al. 2025, A&A, 694, A322
Freedman, W. L., Madore, B. F., Hoyt, T. J., et al. 2025, ApJ, 985, 203
Ge, F., Millea, M., Camphuis, E., et al. 2025, Phys. Rev. D, 111, 083534
Gerbino, M., & Lattanzi, M. 2017, Front. Phys., 5, 70
Gil-Marín, H., Bautista, J. E., Paviot, R., et al. 2020, MNRAS, 498, 2492
Hahn, C., Wilson, M. J., Ruiz-Macias, O., et al. 2023, AJ, 165, 253
Handley, W., & Lemos, P. 2019, Phys. Rev. D, 100, 023512
Harris, C. R., Millman, K. J., van der Walt, S. J., et al. 2020, Nature, 585, 357
Herold, L., & Karwal, T. 2025, ArXiv e-prints [arXiv:2506.12004]
Hou, J., Sánchez, A. G., Ross, A. J., et al. 2021, MNRAS, 500, 1201
Howlett, C., Ross, A. J., Samushia, L., Percival, W. J., & Manera, M. 2015, MNRAS, 449, 848
Hunter, J. D. 2007, Comput. Sci. Eng., 9, 90
Ivanov, M. M., Simonović, M., & Zaldarriaga, M. 2020, Phys. Rev. D, 101, 083504
Kaiser, N., Wilson, G., & Luppino, G.A. 2000, ArXiv e-prints [arXiv:astro-ph/0003338]
Kamionkowski, M., & Riess, A. G. 2023, Ann. Rev. Nucl. Part. Sci., 73, 153
Katrin, C., Aker, M., et al. 2025, Science, 388, 180
Kovač, M., Nicola, A., Bucko, J., et al. 2025, JCAP, 2025, 046
Lange, J. U. 2023, MNRAS, 525, 3181
Lesgourgues, J., & Pastor, S. 2006, Phys. Rep., 429, 307
Lewis, A. 2025, JCAP, 2025, 025
Lewis, A., & Chamberlain, E. 2025, JCAP, 2025, 065
Lewis, A., Challinor, A., & Lasenby, A. 2000, ApJ, 538, 473
Li, S.-S., Hoekstra, H., Kuijken, K., et al. 2023a, A&A, 679, A133
Li, S.-S., Kuijken, K., Hoekstra, H., et al. 2023b, A&A, 670, A100
Li, X., Zhang, T., Sugiyama, S., et al. 2023c, Phys. Rev. D, 108, 123518
Linder, E. V. 2003, Phys. Rev. Lett., 90, 091301
Louis, T., La Posta, A., Atkins, Z., et al. 2025, JCAP, 2025, 062
Loureiro, A., Cuceu, A., Abdalla, F. B., et al. 2019, Phys. Rev. Lett., 123, 081301
Madhavacheril, M. S., Qu, F. J., Sherwin, B. D., et al. 2024, ApJ, 962, 113
Mead, A. J., Brieden, S., Tröster, T., & Heymans, C. 2021, MNRAS, 502, 1401
Miller, L., Heymans, C., Kitching, T. D., et al. 2013, MNRAS, 429, 2858
Naess, S., Guan, Y., Duivenvoorden, A. J., et al. 2025, JCAP, 2025, 061
Neveux, R., Burtin, E., de Mattia, A., et al. 2020, MNRAS, 499, 210
Omori, Y., Baxter, E. J., Chang, C., et al. 2023, Phys. Rev. D, 107, 023529
Pan, Z., Bianchini, F., Wu, W. L. K., et al. 2023, Phys. Rev. D, 108, 122005
Perlmutter, S., Aldering, G., Goldhaber, G., et al. 1999, ApJ, 517, 565
Planck Collaboration V. 2020, A&A, 641, A5
Planck Collaboration VI. 2020, A&A, 641, A6
Prince, H., & Dunkley, J. 2019, Phys. Rev. D, 100, 083502
Qu, F. J., Sherwin, B. D., Madhavacheril, M. S., et al. 2024, ApJ, 962, 112
Qu, F. J., Ge, F., Wu, W. L. K., et al. 2026, Phys. Rev. Lett., 136, 021001
Raichoor, A., Moustakas, J., Newman, J. A., et al. 2023, AJ, 165, 126
Raveri, M., Zacharegkas, G., & Hu, W. 2020, Phys. Rev. D, 101, 103527
Reischke, R., & Hagstotz, S. 2025, OJA, submitted [arXiv:2507.17742]
Reischke, R., Unruh, S., Asgari, M., et al. 2025, A&A, 699, A124
Riess, A. G., Filippenko, A. V., Challis, P., et al. 1998, AJ, 116, 1009
Riess, A. G., Casertano, S., Yuan, W., Macri, L. M., & Scolnic, D. 2019, ApJ, 876, 85
Robertson, N. C., Alonso, D., Harnois-Déraps, J., et al. 2021, A&A, 649, A146
Ross, A. J., Samushia, L., Howlett, C., et al. 2015, MNRAS, 449, 835
Sailer, N., Farren, G. S., Ferraro, S., & White, M. 2026, Phys. Rev. Lett., 136, 081002
Samuroff, S., Mandelbaum, R., Blazek, J., et al. 2023, MNRAS, 524, 2195
Schaller, M., Schaye, J., Kugel, R., Broxterman, J. C., & van Daalen, M. P. 2025, MNRAS, 539, 1337
Schaye, J., Kugel, R., Schaller, M., et al. 2023, MNRAS, 526, 4978
Schmidt, B. P., Suntzeff, N. B., Phillips, M. M., et al. 1998, ApJ, 507, 46
Schneider, P., Eifler, T., & Krause, E. 2010, A&A, 520, A116
Schöneberg, N., Abellán, G. F., Sánchez, A. P., et al. 2022, Phys. Rep., 984, 1
Scolnic, D., Brout, D., Carr, A., et al. 2022, ApJ, 938, 113
Secco, L. F., Samuroff, S., Krause, E., et al. 2022, Phys. Rev. D, 105, 023515
Skilling, J. 2006, Bayesian Anal., 1, 833
Spurio Mancini, A., Piras, D., Alsing, J., Joachimi, B., & Hobson, M. P. 2022, MNRAS, 511, 1771
Steinhardt, C. L., Phillips, P., & Wojtak, R. 2025, ArXiv e-prints [arXiv:2504.03829]
Stölzner, B., Wright, A. H., Asgari, M., et al. 2025, A&A, 702, A169
Stölzner, B., Reischke, R., Grasso, M., et al. 2026, A&A, 707, A323
Tamone, A., Raichoor, A., Zhao, C., et al. 2020, MNRAS, 499, 5527
Terasawa, R., Takahashi, R., Nishimichi, T., & Takada, M. 2022, Phys. Rev. D, 106, 083504
Tereno, I., Schimd, C., Uzan, J.-P., et al. 2009, A&A, 500, 657
Toomey, M. W., Montefalcone, G., McDonough, E., & Freese, K. 2025, ArXiv e-prints [arXiv:2509.13318]
Tröster, T., Asgari, M., Blake, C., et al. 2021, A&A, 649, A88
Tröster, T., Mead, A. J., Heymans, C., et al. 2022, A&A, 660, A27
van den Busch, J. L., Wright, A. H., Hildebrandt, H., et al. 2022, A&A, 664, A170
Van Waerbeke, L., Mellier, Y., Erben, T., et al. 2000, A&A, 358, 30
Virtanen, P., Gommers, R., Oliphant, T. E., et al. 2020, Nat. Methods, 17, 261
Wittman, D. M., Tyson, J. A., Kirkman, D., Dell'Antonio, I., & Bernstein, G. 2000, Nature, 405, 143
Wong, K. C., Suyu, S. H., Chen, G. C. F., et al. 2020, MNRAS, 498, 1420
Wright, A. H., Kuijken, K., Hildebrandt, H., et al. 2024, A&A, 686, A170
Wright, A. H., Hildebrandt, H., van den Busch, J. L., et al. 2025a, A&A, 703, A144
Wright, A. H., Stölzner, B., Asgari, M., et al. 2025b, A&A, 703, A158
Yao, J., Shan, H., Zhang, P., et al. 2023, A&A, 673, A111
Ye, G., Martinelli, M., Hu, B., & Silvestri, A. 2025, Phys. Rev. Lett., 134, 181002
Yoon, M., Hoekstra, H., Li, S.S., et al. 2025, A&A, submitted [arXiv:2510.01122]
Zhou, R., Dey, B., Newman, J. A., et al. 2023, AJ, 165, 58
Zuntz, J., Paterno, M., Jennings, E., et al. 2015, A&C, 12, 45

[1] Argelander-Institut für Astronomie, Universität Bonn, Auf dem Hügel 71, D-53121 Bonn, Germany

[2] Ruhr University Bochum, Faculty of Physics and Astronomy, Astronomical Institute (AIRUB), German Centre for Cosmological Lensing, 44780 Bochum, Germany
[3] Department of Physics and Astronomy, University College London, Gower Street, London WC1E 6BT, United Kingdom
[4] School of Mathematics, Statistics and Physics, Newcastle University, Herschel Building, NE1 7RU Newcastle-upon-Tyne, United Kingdom
[5] Center for Theoretical Physics, Polish Academy of Sciences, al. Lotników 32/46, 02-668 Warsaw, Poland
[6] Institute for Theoretical Physics, Utrecht University, Princetonplein 5, 3584 CC Utrecht, The Netherlands
[7] Leiden Observatory, Leiden University, P.O. Box 9513, 2300 RA Leiden, The Netherlands
[8] Institut de Física d'Altes Energies (IFAE), The Barcelona Institute of Science and Technology, Campus UAB, 08193 Bellaterra (Barcelona), Spain
[9] Institute for Astronomy, University of Edinburgh, Royal Observatory, Blackford Hill, Edinburgh EH9 3HJ, United Kingdom
[10] Centro de Investigaciones Energéticas, Medioambientales y Tecnológicas (CIEMAT), Av. Complutense 40, E-28040, Madrid, Spain
[11] Kavli Institute for Particle Astrophysics and Cosmology, Stanford University, Stanford, CA 94305, USA
[12] SLAC National Accelerator Laboratory, Menlo Park, CA 94025, USA
[13] Universität Innsbruck, Institut für Astro- und Teilchenphysik, Technikerstr. 25/8, 6020 Innsbruck, Austria
[14] The Oskar Klein Centre, Department of Physics, Stockholm University, AlbaNova University Centre, SE-106 91 Stockholm, Sweden
[15] Imperial Centre for Inference and Cosmology (ICIC), Blackett Laboratory, Imperial College London, Prince Consort Road, London SW7 2AZ, United Kingdom
[16] Department of Physics, University of Oxford, Denys Wilkinson Building, Keble Road, Oxford OX1 3RH, United Kingdom
[17] Donostia International Physics Center, Manuel Lardizabal Ibilbidea, 4, 20018 Donostia, Gipuzkoa, Spain
[18] Dipartimento di Fisica e Astronomia "Augusto Righi" – Alma Mater Studiorum Università di Bologna, Via Piero Gobetti 93/2, I-40129 Bologna, Italy
[19] Istituto Nazionale di Astrofisica (INAF) – Osservatorio di Astrofisica e Scienza dello Spazio (OAS), Via Piero Gobetti 93/3, I-40129 Bologna, Italy
[20] Istituto Nazionale di Fisica Nucleare (INFN) – Sezione di Bologna, Viale Berti Pichat 6/2, I-40127 Bologna, Italy
[21] Department of Physics "E. Pancini" University of Naples Federico II C.U. di Monte Sant'Angelo Via Cintia, 21 ed. 6, 80126 Naples, Italy
[22] INAF – Osservatorio Astronomico di Padova, Via dell'Osservatorio 5, 35122 Padova, Italy
[23] Institute for Particle Physics and Astrophysics, ETH Zürich, Wolfgang-Pauli-Strasse 27, 8093 Zürich, Switzerland
[24] Institute for Computational Cosmology, Ogden Centre for Fundamental Physics – West, Department of Physics, Durham University, South Road, Durham DH1 3LE, United Kingdom
[25] Centre for Extragalactic Astronomy, Ogden Centre for Fundamental Physics – West, Department of Physics, Durham University, South Road, Durham DH1 3LE, United Kingdom
[26] Graduate School of Science, Nagoya University, Furocho, Chikusa-ku, Nagoya, Aichi 464-8602, Japan

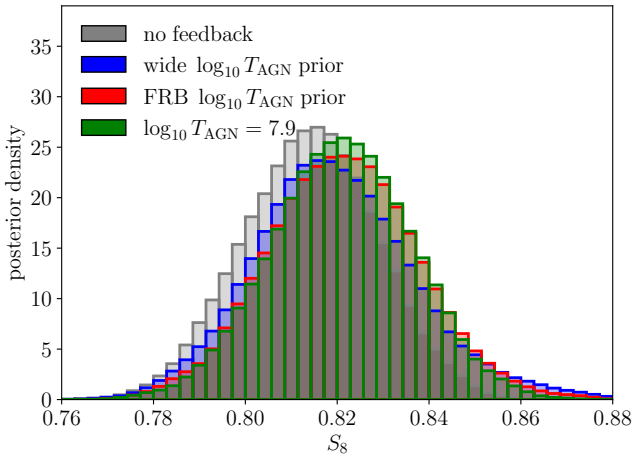

Fig. A.1. Marginal posterior distribution of S_8 for different prior choices for the feedback parameter $\log_{10} T_{\rm AGN}$, only using KiDS-Legacy cosmic shear data.

Appendix A: Feedback prior

The feedback parameter, $\log_{10} T_{\rm AGN}$, is barely constrained (compare Table 4). If at all, one can find an upper limit for $\log_{10} T_{\rm AGN}$ for some probe combinations. Since large $\log_{10} T_{\rm AGN}$ corresponds to stronger feedback, this is indicative of a ceiling to the amount of feedback. This is, of course, only true for the shape of the power spectrum suppression facilitated by $\log_{10} T_{\rm AGN}$ and for the summary statistic used. Broxterman et al. (2025) for example, reconstruct the matter power spectrum using a different summary statistic, $\xi_\pm$, and find a somewhat larger suppression than indicated by the posterior for $\log_{10} T_{\rm AGN}$.

Since the influence of S_8 on the extensions studied here was already established in the main text, the main question we can still address is whether different prior choices on $\log_{10} T_{\rm AGN}$ influence S_8. To this end, we run four additional chains using only the KiDS-Legacy data, changing the prior range of $\log_{10} T_{\rm AGN}$ to a wide prior: $\log_{10} T_{\rm AGN} \in [6.8, 9.6]$, (compare to the fiducial prior adopted in Table 2: $\log_{10} T_{\rm AGN} \in [7.3, 8.3]$). This prior range allows the suppression of the matter power spectrum to exceed unity; that is, the power will be enhanced. This happens if $\log_{10} T_{\rm AGN} < 7.3$ and affects only scales with $k > 1\,h\,{\rm Mpc}^{-1}$. However, the effect can reach 10% at $k = 10\,h\,{\rm Mpc}^{-1}$. Furthermore, this broad prior is much wider than what HMCODE2020 has been calibrated on, so extrapolation might not give the most realistic results. However, we only want to show that we are not sensitive to that choice. Additionally, we use recent constraints on $\log_{10} T_{\rm AGN}$ from Fast Radio Bursts (FRBs, Reischke & Hagstotz 2025) to provide a somewhat tighter prior, in particular favouring stronger feedback models over the KiDS data. These constraints are also consistent with previous analyses using KiDS-1000 and the thermal Sunyaev-Zel'dovich effect (Tröster et al. 2022).

The result of this exercise is shown in Fig. A.1, illustrating that S_8 is very stable with respect to the prior choices. The tighter prior on $\log_{10} T_{\rm AGN}$ increases S_8 slightly and improves the constraints marginally. This is due to the modest preference for stronger feedback among the FRBs, which requires a larger S_8. Lastly, we check the posterior of S_8 for two other cases: firstly, for a fixed value of $\log_{10} T_{\rm AGN} = 7.9$, which corresponds to the value found in Reischke & Hagstotz (2025) and is consistent with the suppression measured in Bigwood et al. (2024), Kovač et al. (2025) and the $f_{\rm gas} - 8\sigma$ FLAMINGO simulation (Schaye et al. 2023; Schaller et al. 2025), that is fairly strong feedback. Secondly, we assume no feedback and infer S_8 from a pure CDM power spectrum. The results are shown as a green and grey histogram, respectively. In Dark Energy Survey and Kilo-Degree Survey Collaboration (2023) it was already shown that COSEBIs within the angular scales used here are expected to be rather insensitive to feedback. As before, we observe that larger feedback shifts S_8 slightly higher. The fact that we do not have to marginalise over the feedback results in marginally tighter constraints on S_8.

In conclusion, this plot shows that the fiducial analysis of KiDS-Legacy and, in combination with the results shown here, also the extended cosmological analysis are not influenced by the prior on the feedback parameter when using COSEBIs as a summary statistic, in line with Wright et al. (2025b).

Appendix B: Full cosmological posteriors

In this Appendix, we show the posterior distributions of the cosmological parameters and the feedback parameter $\log_{10} T_{\rm AGN}$. Figs. B.1a to B.1d show the credible regions for the three extensions for KiDS-Legacy, lensing, low-z and low-z+CMB (compare Table 1), respectively.

Here, one can see a few trends discussed in the main text. Figs. B.1a to B.1b e.g. show that allowing the neutrino mass to vary leads to more probability mass at lower $n_{\rm s}$ in Fig. B.1a, thus lowering S_8 slightly. However, this degeneracy is broken by introducing any of the external probes studied here; large values of $n_{\rm s}$ become excluded. In Fig. B.1b, one can see that in ΛCDM, gravitational lensing can constrain the Hubble constant slightly (black contour). This is possible because the range of scales tested by CMB lensing and cosmic shear is large enough to resolve the peak of the power spectrum and the transition from linear to non-linear scales, both of which depend on h.

Fig. B.1d shows the effect of opening up the parameter space to dynamical dark energy when using the CMB, as the strong degeneracy between $\Omega_{\rm m}$ is exposed in this case. In ΛCDM, this is not visible since the expansion history is fixed by the combination of the CMB and BAO, limiting the range of $\Omega_{\rm m}$ values. This allows the exploration of low values of h that are, in principle, rejected by our prior choices (see Table 2). For chains including the CMB and dynamical dark energy, however, we allow for a wider h prior to discover the full shape of the posterior as driven by the likelihood. Tröster et al. (2021) found a similar situation for Ω_K; however, in this work, this is remedied by the inclusion of additional data, thereby removing the slight skewness towards negative Ω_K in the CMB. In fact, we find consistent results with the analysis presented in Camphuis et al. (2025), with $\Omega_K > 0$ at 2.6σ. This, however, does not warrant a model preference as we show in Table 3. It is noteworthy that the addition of SNe from Pantheon+ blocks the high $\Omega_{\rm m}$ and low h part of the parameter space again.

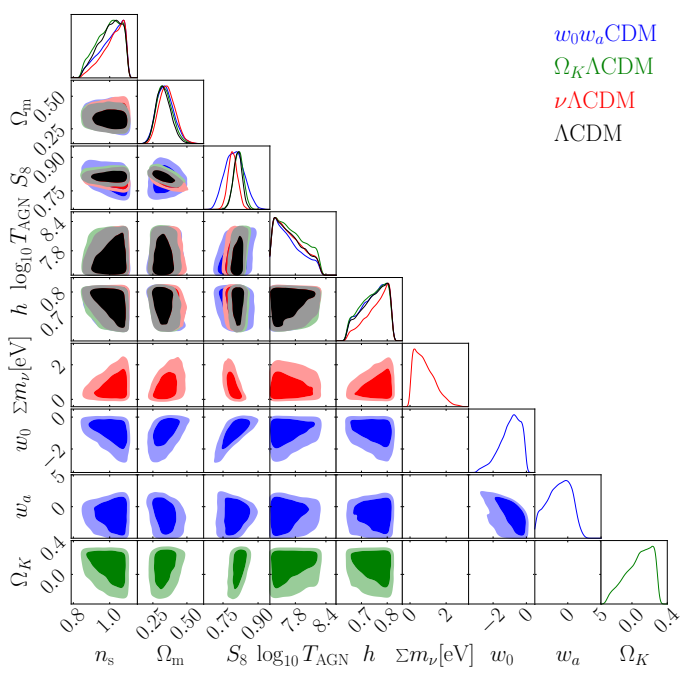

(a) KiDS-Legacy

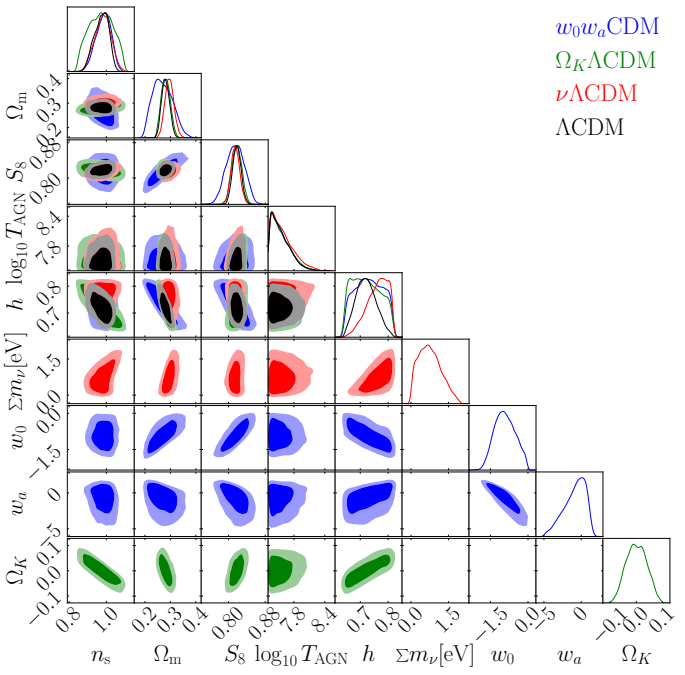

(b) KiDS+DES Y3+CMB(lensing)

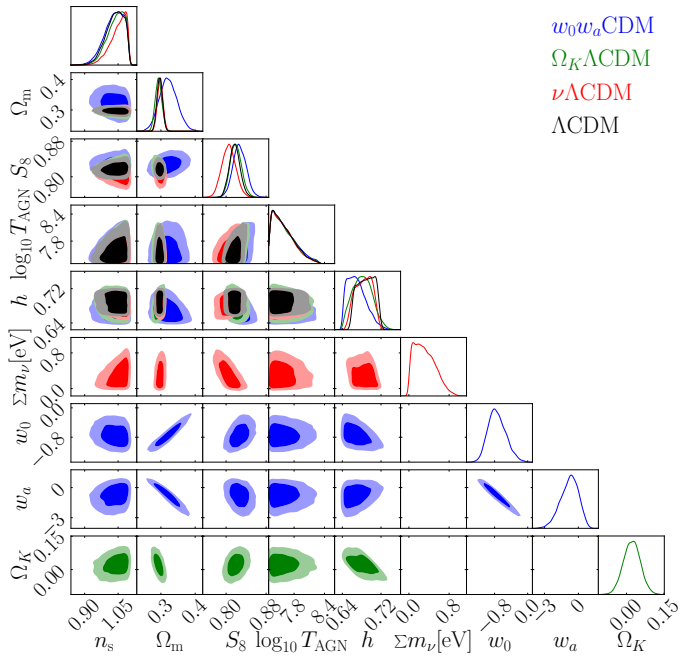

(c) KiDS+DES Y3+DESI BAO+eBOSS RSD (low-z)

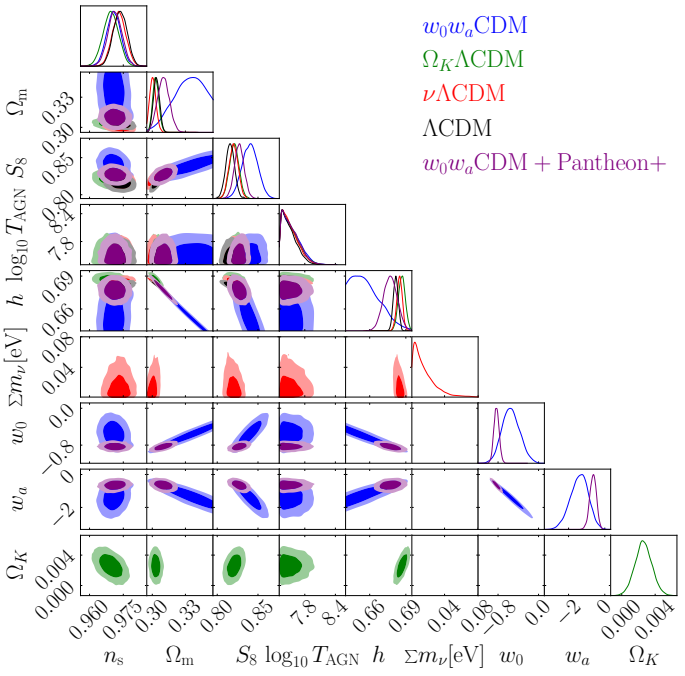

(d) low-z+CMB(+Pantheon+, purple)

Fig. B.1. Marginal constraints for the full set of cosmological parameters and the feedback parameter for all probe combinations and model extensions discussed in this work.